Seismic acquisition design based on full-wavefield migration

Revelo-Obando, Billy; Blacquière, Gerrit

DOI
10.1190/geo2022-0313.1

Publication date
2023

Document Version
Final published version

Published in
Geophysics

GEOPHYSICS®

Seismic acquisition design based on full-wavefield migration

Journal:	*Geophysics*
Manuscript ID	GEO-2022-0313.R2
Manuscript Type:	Technical Paper
Keywords:	acquisition, survey design, imaging, optimization
Manuscript Focus Area:	Seismic Data Acquisition

DOI:10.1190/geo2022-0313.1

Seismic acquisition design based on full-wavefield migration

Billy Revelo-Obando* **and Gerrit Blacquière***

**Delft University of Technology,*

Department of Geoscience and Engineering,

Stevinweg 1, 2628 CN,

Delft, The Netherlands.

E-mail: b.a.reveloobando@tudelft.nl (corresponding author);

g.blacquiere@tudelft.nl.

(January 25, 2023)

GEO-2022-0313.R2

Running head: **Acquisition design based on FWM**

Seismic acquisition design based on full-wavefield migration

(January 25, 2023)

GEO-2022-0313.R2

Running head: **Acquisition design based on FWM**

ABSTRACT

The ultimate goal in survey design is to obtain the acquisition parameters that enable acquiring the most affordable data that fulfills certain image quality requirements. We propose a method that allows optimization of the receiver geometry for a fixed source distribution. The former is parameterized with a receiver density function that determines the number of receivers per unit area. We optimize this receiver density function through an iterative gradient descent scheme that minimizes the difference between the image obtained with the current acquisition geometry and a reference image. The reference image is obtained from prior subsurface information that is assumed to be available. We tested the method with different subsurface models. The results show that the acquisition geometry is optimized according to the complexity of each subsurface model. The receivers are moved towards the areas where more data is needed for obtaining better imaging.

INTRODUCTION

The goal of seismic survey design is to find the acquisition parameters that - after a certain data-processing sequence - lead to a certain image quality, while fulfilling economic, time and environmental constraints.

In traditional acquisition geometries, seismic sources and receivers are laid out in (straight) lines. The spacing between stations within a line and the separation between lines is chosen to achieve certain common midpoint (CMP) properties: resolution, offset distribution and trace multiplicity (Vermeer, 2012). Ideally, without the presence of noise, the expected resolution of a seismic image can be computed through the seismic velocities in the subsurface and the bandwidth of seismic data. However, in real-world acquisition, often a higher trace multiplicity is required to obtain an adequate signal-to-noise ratio (SNR).

The source and receiver sampling of an unaliased acquisition geometry would satisfy the Nyquist-Shannon criterion (at least two samples per smallest wavelength, which may be related to a noise signal). However, in practice this is not feasible due to associated acquisition and processing costs. In marine acquisition for example, acquisition with ocean bottom nodes has gained popularity due to the flexibility of the source location with respect to the location of the receivers. This provides denser source sampling, longer offsets and better angle distribution than in the case of streamer acquisition when a single vessel is used (Regone, 2006), for example. It also provides a better coupling with the seafloor and vector fidelity (Alerini et al., 2009). However, this type of receivers has a high cost compared to marine streamer

cables. For this reason, their optimal positioning is critical for reducing costs while obtaining a high quality image of the target zone.

Additionally to the limitations of a survey design arising due to the presence of noise, a complex subsurface may hinder the illumination-and-detection properties of the survey. For example salt structures or karst topographies, can reduce the illumination of underlying targets of economical interest (Muerdter and Ratcliff, 2001). It means that the expected resolution of the survey design is affected by the complexity of the subsurface: the image of the target zone can be deficient while other zones of less interest get a better image quality.

In areas where seismic exploration has been carried out previously, legacy data as well as corresponding subsurface models are available. These can be used in the design of a future survey to take the particular subsurface properties into consideration, such as the major, multiple-generating reflectors. This has been undertaken through the use of modeling and imaging studies, where an initial geometry is manually updated to achieve better illumination in the target zones (Singh et al., 2016; Theriot et al., 2014). However, in this type of experimental survey design, the theory is not directly linked with the outcome of the experiment (Maurer et al., 2010). New approaches in survey design make use of deep learning to optimize survey design parameters for blended acquisition (Nakayama et al., 2019). Here the computational cost of modeling multiple geometries is avoided by selecting the most suitable with the aid of neural networks.

In some complex subsurface scenarios, multiple reflections could play an important

role in the acquisition design depending on whether they are considered as signal or as noise. In the first case, full-wavefield imaging algorithms can make use of multiple reflections for the reflectivity estimation process as the latter can provide illumination that is supplementary to the illumination by primary reflections. In the second case, the multiples must be eliminated prior to imaging.

Methods such as the focal beam analysis (Berkhout et al., 2001; Volker et al., 2001) can predict the resolution and illumination properties of an acquisition geometry for a single point in a complex subsurface. However, the acquisition parameters have to be manually tuned to improve the deficiencies of the survey design.

We developed an iterative algorithm that optimizes the acquisition geometry in a survey area for which some prior knowledge is available and that assumes Full-Wavefield Migration (FWM, Davydenko and Verschuur (2017)) to be used as the processing algorithm. We choose FWM as it makes use of multiple reflections for imaging, potentially increasing the subsurface illumination compared to primaries-only migration algorithms (Davydenko and Verschuur, 2018; Revelo-Obando and Blacquière, 2021). This could relax spatial sampling requirements, which would save costs in sparse acquisition scenarios such as ocean-bottom node acquisition. In this paper we limit ourselves to computing the locations of a fixed number of receivers. This means that we aim to distribute the available receivers optimally in a spatial sense.

The receiver geometry is parameterized through a receiver density function that determines the number of receivers per unit area. The quality of an acquisition geometry is evaluated through a least-squares target function that compares the image

obtained after each iteration with a reference image. If the quality criterion is not satisfied, the receiver density function is updated through a gradient descent scheme and the iterative process continues.

This paper is divided as follows: first, the framework of survey design and FWM is described. Then the receiver geometry parameterization and the target function are introduced. Subsequently, the optimization algorithm is discussed, including the gradient descent scheme for the receiver density function optimization. Then three examples are presented to demonstrate the performance of the algorithm. The paper ends with a discussion and conclusions.

THEORY

Framework of survey design

We describe 3D seismic data with the matrix notation proposed by Berkhout (1982). For one frequency component, a seismic dataset can be formulated as:

$$\mathbf{P}^{-}(z_d, z_s) = \mathbf{D}(z_d)\mathbf{X}^{-}(z_d, z_s)\mathbf{S}^{+}(z_s). \tag{1}$$

where matrix $\mathbf{P}^{-}$ represents the upgoing acoustic pressure wavefields recorded by receivers at depth level z_d, generated by sources at depth level z_s. Each matrix element P^{-}_{jk} is a complex number that contains the amplitude and phase information of the trace recorded by receiver j due to source k for the frequency component under consideration. Matrices $\mathbf{S}^{+}$ and $\mathbf{D}$ are the source and receiver matrix respectively. Together they describe the survey geometry as well as the source and receiver properties

(directivity, sensitivity, spectral properties, etc.). Matrix $\mathbf{X}^-$ represents the transfer operator of the subsurface, and contains all propagation and (multiple-)reflection effects. It can be considered to be the ideal seismic data set, i.e., with densely sampled carpet shooting and carpet detection with unit sources and unit detectors, respectively. The + and - superscripts indicate the down- and upgoing wavefield direction, respectively. As mentioned, in this research we assume that $\mathbf{X}^-(z_d, z_s)$ can be modeled, e.g., using a subsurface model based on prior knowledge such as obtained from legacy data.

If sources and detectors are both located at the surface z_0, i.e., $z_s = z_d = z_0$, equation 1 becomes:

$$\mathbf{P}^-(z_0, z_0) = \mathbf{D}(z_0)\mathbf{X}^-(z_0, z_0)\mathbf{S}^+(z_0). \tag{2}$$

For the case that the sources are ideal and perfectly sampled, $\mathbf{S}^+(z_0)$ equals the identity matrix $\mathbf{I}^+(z_0)$ and equation 2 becomes:

$$\mathbf{P}^-(z_0, z_0) = \mathbf{D}(z_0)\mathbf{X}^-(z_0, z_0). \tag{3}$$

The modeling of $\mathbf{X}^-(z_0, z_0)$ could be performed with any modeling engine, e.g. with finite-difference modeling. Our modeling method is Full-wavefield modeling (FWMod) (Berkhout, 2014a). It is recursive in depth as well as iterative. It is also the modeling engine used in FWM, described in the next section. In this way of modeling, the up- and down-going wavefields $\mathbf{X}_i^-(z_n, z_0)$ and $\mathbf{X}_i^+(z_n, z_0)$ at depth level z_n are computed for all iterations i. Here, n ranges from 0 to N, with z_N being the maximum depth of interest. These iterations are called round trips, and each round trip adds

one additional order of multiple reflections. This means that the primary reflections are obtained in the first round trip, the primaries plus the first order multiples in the second, and so on. One round trip consists of a downgoing step ($n = 1, 2, ..., N$) and an upgoing step ($N = N-1, N-2, ..., 0$) which can be formulated as:

$$\mathbf{X}_i^+(z_n, z_0) = \sum_{m=1}^{n-1} \mathbf{U}^+(z_n, z_m)\mathbf{R}^{\cap}(z_m)\mathbf{X}_{i-1}^-(z_m, z_0) + \mathbf{U}^+(z_n, z_0)\mathbf{I}^+(z_0), \tag{4a}$$

$$\mathbf{X}_i^-(z_n, z_0) = \sum_{m=n+1}^{N} \mathbf{U}^-(z_n, z_m)\mathbf{R}^{\cup}(z_m)\mathbf{X}_i^+(z_m, z_0). \tag{4b}$$

As introduced earlier, identity matrix $\mathbf{I}^+(z_0)$ represents the collection of ideal downgoing source wavefields. Matrices $\mathbf{R}^{\cap}(z_m)$ and $\mathbf{R}^{\cup}(z_m)$ are the up-down and down-up, angle-dependent reflection operators at depth level z_m. Matrices $\mathbf{U}^-$ and $\mathbf{U}^+$ are the upgoing and downgoing full wavefield propagators respectively. They are computed as follows:

$$\mathbf{U}^+(z_n, z_m) = \left[\prod_{k=n-1}^{m+1} \mathbf{W}^+(z_{k+1}, z_k)\mathbf{T}^+(z_k)\right] \mathbf{W}^+(z_{m+1}, z_m), \tag{5a}$$

$$\mathbf{U}^-(z_n, z_m) = \left[\prod_{k=n+1}^{m-1} \mathbf{W}^-(z_{k-1}, z_k)\mathbf{T}^-(z_k)\right] \mathbf{W}^-(z_{m-1}, z_m), \tag{5b}$$

where $\mathbf{W}^+(z_{k+1}, z_k)$ is the downward wavefield propagation operator from depth level z_k to depth level z_{k+1}; $\mathbf{W}^-(z_{k-1}, z_k)$ is the upward wavefield propagation operator from depth level z_k to depth level z_{k-1}; $\mathbf{T}^+(z_k)$ is the transmission operator of the downgoing wavefield crossing depth level z_k from above; $\mathbf{T}^-(z_k)$ is the transmission operator of the upgoing wavefield crossing depth level z_k from below.

From equations 5a and 5b it is clear that operator $\mathbf{U}^+(z_n, z_m)$ includes all propagation and transmission effects of wavefields propagating in the downward direction

from depth level z_m to depth level z_n, and so does operator $\mathbf{U}^-(z_n, z_m)$ for wavefields propagating in the upward direction. The use of this type of modeling allows to specify reflectivity and transmissivity independently from propagation velocity. The output of this scheme, after L iterations, is the modeled, perfectly sampled data, $\mathbf{X}_L^-(z_0, z_0) = \mathbf{X}^-(z_0, z_0)$, which can be turned into more realistic data via multiplication with $\mathbf{D}(z_0)$, see equation 3 (still under the assumption of a perfect source distribution).

In the acoustic case, the transmission operators can be described in terms of the reflectivity:

$$\mathbf{T}^+(z_k) = \mathbf{I} + \mathbf{R}^\cup(z_k), \tag{6a}$$

$$\mathbf{T}^-(z_k) = \mathbf{I} + \mathbf{R}^\cap(z_k). \tag{6b}$$

This means that the acoustic assumption reduces the number of independent reflection and transmission matrices from four to two. In addition, if reflection and transmission are assumed to be angle-independent, these matrices become diagonal matrices, even further reducing the number of parameters.

Reflectivity estimation with FWM

In seismic migration, the objective is to estimate the reflectivity of the subsurface given the seismic data and a propagation velocity model. The reflectivity matrices $\mathbf{R}^\cup$ and $\mathbf{R}^\cap$, estimated by FWM (Berkhout, 2014b; Davydenko and Verschuur, 2017), are obtained through an iterative process where the target function $J_{\Delta,i}$ at iteration

i is minimized. Its expression is:

$$J_{\Delta,i}(z_0,z_0) = \sum_{\omega} tr\left(\Delta\mathbf{P}_i(z_0,z_0)\Delta\mathbf{P}_i(z_0,z_0)^H\right), \tag{7}$$

where $\Delta\mathbf{P}_i(z_0,z_0)$ represents the data residual at iteration i. It is defined as follows:

$$\Delta\mathbf{P}_i(z_0,z_0) = \mathbf{D}_i(z_0)\Delta\mathbf{X}_i^-(z_0,z_0), \text{with} \tag{8a}$$

$$\Delta\mathbf{X}_i^-(z_0,z_0) = \mathbf{X}^-(z_0,z_0) - \mathbf{X}_i^-(z_0,z_0), \tag{8b}$$

where, as we shall see later, receiver matrix $\mathbf{D}_i(z_0)$ depends on iteration i. In FWM, the reflectivity operators are updated at each iteration through an iterative gradient descent scheme. Therefore, update directions $\delta\mathbf{R}_i^{\cup}$ and $\delta\mathbf{R}_i^{\cap}$ are needed. These are found by moving along the direction of steepest descent, which is the direction along which $J_{\Delta,i}$ is minimized. Therefore, the reflectivity update directions are the derivatives of $J_{\Delta,i}$ with respect to $\mathbf{R}^{\cup}$ and $\mathbf{R}^{\cap}$ respectively:

$$\delta\mathbf{R}_i^{\cup}(z_n) = |f|^2\left[\mathbf{U}_i^-(z_0,z_n)\right]^H\Delta\mathbf{P}_i(z_0,z_0)\left[\mathbf{X}_i^+(z_n,z_0)\right]^H, \tag{9a}$$

$$\delta\mathbf{R}_i^{\cap}(z_n) = |f|^2\left[\mathbf{U}_i^{\cup}(z_0,z_n)\right]^H\Delta\mathbf{P}_i(z_0,z_0)\left[\mathbf{X}_{i-1}^-(z_n,z_0)\right]^H, \tag{9b}$$

for n=1:N, where $f = f(\omega)$ is a weighting factor that partially compensates for the wavelet signature on the data. The full-wavefield propagation operator $\mathbf{U}_i^{\cup}(z_0,z_n)$ is defined as:

$$\mathbf{U}_i^{\cup}(z_0,z_n) = \sum_{m=n+1}^{N}\mathbf{U}_i^-(z_0,z_m)\mathbf{R}_i^{\cup}(z_m)\mathbf{U}_i^+(z_m,z_n). \tag{10}$$

For practical reasons, we will now introduce two approximations that simplify our theory and the subsequent computer implementation. Rather than considering the reflectivity to be angle dependent, we continue with the angle independent reflection

coefficient for which we take the angle-averaged value. For this case, the reflectivity update direction at each depth level is computed according to:

$$\delta\overline{\mathbf{R}}_i^{\cup}(z_n) = diag\left\{\sum_{\omega}\delta\mathbf{R}_i^{\cup}(z_n)\right\}, \tag{11a}$$

$$\delta\overline{\mathbf{R}}_i^{\cap}(z_n) = diag\left\{\sum_{\omega}\delta\mathbf{R}_i^{\cap}(z_n)\right\}, \tag{11b}$$

where $diag\{\mathbf{M}\}$ clears all off-diagonal elements of matrix $\mathbf{M}$ and where the overbar indicates the angle-independent reflectivity approximation. The summation over ω, corresponding to an inverse FFT from frequency to time for $t = 0$ s only, is applied to implement the imaging principle. The second approximation is that we assume the down-up and up-down reflection coefficients to be each other's opposite (small-angle approximation). Introducing this approximation means that we may combine the two for the computation of the update direction. The joint reflectivity update direction is optimized for preconditioning as follows:

$$\delta\overline{\mathbf{R}}_i(z_n) = [\mathbf{H}_i(z_n)]^{-1}\left[\delta\overline{\mathbf{R}}_i^{\cup}(z_n) - \delta\overline{\mathbf{R}}_i^{\cap}(z_n)\right], \tag{12}$$

where the diagonal matrix $\mathbf{H}_i$ is an approximation of the Hessian that acts as a spatially varying scaling of the gradient (Staal, 2015). Its elements are defined as:

$$\begin{aligned} H_{kk}(z_n) = &\sum_{\omega}\left\|\mathbf{U}^{-}(x, z_0; x_k, z_n)\right\|^2\left|X_i^{+}(x_k, z_n)\right|^2 \\ &+\sum_{\omega}\left\|\mathbf{U}^{\cup}(x, z_0; x_k, z_n)\right\|^2\left|X_{i-1}^{-}(x_k, z_n)\right|^2, \end{aligned} \tag{13}$$

The step length α_i for the reflectivity update is computed as follows:

$$\alpha_i = \frac{tr[\Delta\mathbf{P}_i^H\Delta\mathbf{P}_r(\delta\overline{\mathbf{R}}_i) + \Delta\mathbf{P}_r^H(\delta\overline{\mathbf{R}}_i)\Delta\mathbf{P}_i]}{tr\left[\Delta\mathbf{P}_r^H(\delta\overline{\mathbf{R}}_i)\Delta\mathbf{P}_r(\delta\overline{\mathbf{R}}_i)\right]}, \tag{14}$$

where $\Delta\mathbf{P}_r(\delta\overline{\mathbf{R}}_i)$ is the linearized wavefield perturbation associated to the update direction $\delta\overline{\mathbf{R}}_i$. It is defined as:

$$\Delta\mathbf{P}_r(\delta\overline{\mathbf{R}}_i) = \sum_n \Big\{ \mathbf{U}_i^-(z_0,z_n)\delta\overline{\mathbf{R}}_i(z_n)\mathbf{X}_i^+(z_n,z_0) + \mathbf{U}_i^{\cup}(z_0,z_n)\delta\overline{\mathbf{R}}_i(z_n)\mathbf{X}_{i-1}^-(z_n,z_0)\Big\}. \tag{15}$$

Finally, the reflectivity, for which we assume $\overline{\mathbf{R}}^{\cup}(z_n) = -\overline{\mathbf{R}}^{\cap}(z_n) = \overline{\mathbf{R}}(z_n)$, is updated according to:

$$\overline{\mathbf{R}}_{i+1}(z_n) = \overline{\mathbf{R}}_i(z_n) + \alpha_i\delta\overline{\mathbf{R}}_i(z_n). \tag{16}$$

In the remainder of this paper we will omit the overbar for notational simplicity. Therefore, matrix $\mathbf{R}$ will represent the angle-independent reflectivity approximation.

METHOD

As mentioned before, we assume that we have fully-sampled, ideal data $\mathbf{X}^-(z_0,z_0)$ available. The aim is to design the optimal receiver matrix $\mathbf{D}$ with the positions of n_d receivers, (located on a predefined grid) within a certain aperture, which gives the practical data $\mathbf{P}^-(z_0,z_0) = \mathbf{D}(z_0)\mathbf{X}^-(z_0,z_0)$. Imaging of $\mathbf{P}^-(z_0,z_0)$ then leads to the optimum reflectivity estimate.

In our iterative algorithm we aim at improving the reflectivity estimate at each iteration by updating the receiver matrix, i.e., the imaging process and the acquisition geometry estimation process go hand in hand. At the end of the process, we have both the optimum reflectivity estimate and the corresponding optimum acquisition geometry.

Assuming ideal point receivers, i.e., with a flat, unit sensitivity, for each frequency component matrix $\mathbf{D}(z_0)$ is a diagonal matrix whose elements are either ones or zeros, indicating the presence or absence of a receiver at a grid position, respectively. Therefore, updating the operator implies adding or removing receivers, i.e. changing ones by zeros and vice versa, while keeping n_d constant. Since it is difficult to formulate this in terms of an update direction and a step length, an intermediate parameterization is required.

Parameterization

We parametrize the receiver geometry with a receiver density function $\mathbf{\Phi}$ (Wu et al., 2022). It determines the number of receivers per unit area at each grid point of the acquisition surface. This function is then translated into matrix $\mathbf{D}$ through a transformation g:

$$\mathbf{D}_i = g(\mathbf{\Phi}_i). \tag{17}$$

In equation 17 we have added the subscript i as in our iterative scheme the receiver density and the receiver matrix will be updated at every iteration. Function $\mathbf{\Phi}_i$ is implemented as a real-valued, diagonal matrix with the same dimensions as matrix $\mathbf{D}_i$. The values of the diagonal elements, between 0 and 1, correspond to the receiver density at the corresponding spatial location. Note that an alternative way of interpreting $\mathbf{\Phi}_i$ is that it contains receivers with a sensitivity anywhere between 0 and 1. In practice - even though such receivers could be produced - this would be inefficient. Therefore, it is desired to only deploy receivers that have maximum sensitivity, which

in our case corresponds to a sensitivity of 1. To translate the receiver density in the locations of such receivers, we use a weighted Voronoi Stippling algorithm (Secord, 2002). First, n_d sampling locations are chosen from the receiver density through a simple rejection sampling algorithm. In this algorithm, a random location is chosen and its corresponding receiver density value is compared to a random value taken from a uniform distribution. If the receiver density is higher than the random value, that location is chosen. This procedure is repeated until n_d locations are selected. Therefore, the higher the value of an element of $\mathbf{\Phi}_i$, the higher the possibility of a receiver being put at that location. Next, after choosing the locations, these are redistributed through Lloyd's algorithm (Lloyd, 1982). This algorithm computes the Voronoi diagram of a set of points, in our case the receiver locations, and shifts their locations to the centroids of the computed Voronoi cells. Finally, the locations are translated into the receiver matrix $\mathbf{D}_i$ by placing a '1' at the corresponding grid location. This is done by approximating the locations found through the Lloyd's algorithm to the closest grid position. Figure 1 shows an example of a linearly increasing receiver density $\mathbf{\Phi}_i$ and the corresponding receiver matrix $\mathbf{D}_i$.

In the remainder of this paper, we will use $\mathbf{\Phi}_i$ and $\mathbf{D}_i$ interchangeably. The former when a continuous variable is needed, and the latter when a discrete variable is required, e.g., for data sampling. It is important to note that the transformation g is non-deterministic. This means that for a single receiver density matrix $\mathbf{\Phi}_i$, multiple realizations of matrix $\mathbf{D}_i$ can be obtained. However, the Voronoi iterations tend to reduce the differences between these realizations.

Target function

Starting with an 'empty' initial reflectivity model $\mathbf{R}_i(z_n) = 0$ for $i = 0$, the first step in our algorithm is to estimate a reflectivity update $\mathbf{R}_{i+1}(z_n)$ with one FWM iteration, using an arbitrary initial receiver geometry $\mathbf{D}_i$ for $i = 0$ and with n_d receivers. The receiver positions of such a geometry could, for instance, be equidistant. Subsequently, we evaluate the quality of the obtained image. We propose a least-squares target function J_R defined as follows:

$$J_{R,i} = \sum_n \|\Delta\mathbf{R}_i(z_n)\|^2, \tag{18a}$$

$$\Delta\mathbf{R}_i(z_n) = \mathbf{R}(z_n) - \mathbf{R}_{i+1}(z_n), \tag{18b}$$

where matrix $\mathbf{R}(z_n)$ represents a reference image at z_n. In our case it is the best possible migration result obtained with a full receiver sampling, i.e., satisfying the Nyquist criterion. Matrix $\mathbf{R}_{i+1}(z_n)$ is the reflectivity update obtained by FWM at iteration i (see equation 16). The residual $\Delta\mathbf{R}_i$ is the difference between the reference image and the estimated one at iteration i. If desired, $\Delta\mathbf{R}_i(z_n)$ could be multiplied with a spatially-varying weighting function to give priority to certain target zones. A threshold ϵ can be established for $J_{R,i}$ as a quality criterion: if $J_{R,i} < \epsilon$, the quality criterion has been met and the iterative process can stop. If the quality criterion is easily reached, e.g., already within a few iterations, one may consider reducing n_d. This could result in a cheaper acquisition design that still fulfills the desired quality requirements. If the quality criterion has not been met, apparently the receiver geometry needs to be further improved (updated) in the subsequent iteration(s), as will be discussed next. In the case that the quality criterion can not be reached, n_d

and/or ϵ could be increased, but we stop when the predefined maximum number of iterations `nit` has been reached.

Gradient descent scheme

We propose to update the receiver density $\mathbf{\Phi}$ through an iterative gradient descent scheme:

$$\mathbf{\Phi}_{i+1} = \mathbf{\Phi}_i + \beta_i \delta\mathbf{\Phi}_i, \tag{19}$$

where $\mathbf{\Phi}_i$ is the current-iteration receiver density, $\delta\mathbf{\Phi}_i$ is the update direction, β_i is the step length, and $\mathbf{\Phi}_{i+1}$ is the updated, next-iteration receiver density. As mentioned, $\mathbf{\Phi}_{i+1}$ is translated into receiver matrix $\mathbf{D}_{i+1}$ through transformation g.

Update direction and step length

The update direction for the receiver density is given by the (conjugate) gradient of target function $J_{R,i}$ (equation 18a) with respect to receiver density $\mathbf{\Phi}$. Hence, the derivative to be computed is:

$$\frac{\partial J_{R,i}}{\partial \mathbf{\Phi}} = \frac{\partial}{\partial \mathbf{\Phi}} \left[\sum_n \left\| \Delta\mathbf{R}_i(z_n) \right\|^2 \right]. \tag{20}$$

As derived in Appendix A, this derivative can be expressed as:

$$\frac{\partial J_{R,i}}{\partial \mathbf{\Phi}} = \sum_n \sum_\omega -2\alpha_i |f|^2 \left[\mathbf{H}_i(x, z_n)\right]^{-1} \Delta\mathbf{P}_r(\Delta\mathbf{R}_i(z_n))[\Delta\mathbf{X}_i^-(z_0, z_0)]^H. \tag{21}$$

This equation contains the correlation between the data residual $\Delta\mathbf{X}_i^-$ and the seismic data $\Delta\mathbf{P}_r$ modeled from the residual image $\Delta\mathbf{R}_i$. Therefore, it can be interpreted as a mapping from the model update to the data space, at the sampling locations where more data is needed.

The update direction is given by the negative conjugate of equation 21:

$$\delta\mathbf{\Phi}_i = -\frac{\partial J^*_{R,i}}{\partial\mathbf{\Phi}}, \tag{22}$$

and the step length is given by (see Appendix B):

$$\beta_i = \frac{(\delta\mathbf{\Phi}_i)^H\delta\mathbf{\Phi}_i}{\left[-2\alpha_i|f|^2\left[\mathbf{H}_i(x,z_n)\right]^{-1}\Delta\mathbf{P}_r(\mathbf{R}_\phi(z_n))[\Delta\mathbf{X}_i^-(z_0,z_0)]^H\right]^H\delta\mathbf{\Phi}_i}, \tag{23}$$

where $\mathbf{R}_\phi(z_n)$ is an image associated with the receiver density update direction and $\Delta\mathbf{P}_r(\mathbf{R}_\phi(z_n))$ is the corresponding wavefield perturbation, similar as with equation 15.

Algorithm

The iterative process to optimize the receiver geometry is summarized in Algorithm 1.

Algorithm 1 Acquisition geometry optimization algorithm

Require: $\mathbf{X}^-(z_0, z_0), \mathbf{R}, \mathbf{D}_0$

for $0 \leq i \leq$ `nit` **do** ▷ Acquisition geometry with `nit` updates

  Compute wavefields $\mathbf{X}_i^+, \mathbf{X}_i^-$

  $\Delta\mathbf{P}_i = \mathbf{D}_i \Delta\mathbf{X}_i^-$ ▷ Apply receiver geometry, compute data residual

  $\mathbf{R}_{i+1} = \mathbf{R}_i + \alpha_i \delta\mathbf{R}_i$ ▷ Update reflectivity

  if $J_{R,i} < \epsilon$ **then** ▷ Evaluate image quality criterion

    Finish

  end if

  $\mathbf{\Phi}_{i+1} = \mathbf{\Phi}_i + \beta_i \delta\mathbf{\Phi}_i$ ▷ Update receiver density

  $\mathbf{D}_{i+1} = g(\mathbf{\Phi}_{i+1})$ ▷ Update receiver geometry

end for

Change number of receivers n_d and restart ▷ If required

RESULTS

We tested our newly developed algorithm for a number of different subsurface models. From these, the reference datasets $\mathbf{X}^-(z_0, z_0)$ were modeled with FWMod, using a Ricker wavelet with a central frequency of 20 Hz and 30 iterations. The corresponding reference reflectivity models ($\mathbf{R}$) were obtained through inversion with FWM using a full receiver sampling (ideal receiver geometry). As mentioned, the source geometry was kept constant for each experiment. In all examples the geometry has a fixed receiver spread.

The first study uses a model that contains three horizontal layers (Figure 2). The source geometry consists of 14 sources uniformly distributed every 180 m. As the model is laterally homogeneous, the optimal receiver geometry is expected to be spatially uniform. To test the algorithm, we start the optimization process with the initial geometry shown in Figure 3a. It consists on $n_d = 41$ receivers, all being located in the left hand side of the model, i.e., far from the expected optimal geometry. After 30 iterations we obtain the receiver density shown in Figure 3c and its corresponding receiver geometry (Figure 3d).

The optimized receiver geometry shown in Figure 3d shows that the receivers are placed almost uniformly along the acquisition surface. However, the receiver density is clearly somewhat higher at the edges of the aperture than in the middle. The reason for this will be discussed later. To test the consistency of the algorithm, we repeat the experiment with a different starting geometry. The same number of receivers are now positioned at the center of the model (Figure 4a) and the algorithm is run again for 30 iterations. The optimized receiver density and corresponding geometry are shown in Figures 4c and 4d.

The optimized receiver geometry shown in Figure 4d closely resembles the one obtained in the previous experiment (Figure 3d) despite the completely different initial geometries. This result confirms the consistency of the algorithm and its robustness to the initial geometry. As in the previous example, the optimized receiver density is slightly higher at the edges than at the center. This means that the corresponding receiver geometries are not completely uniform. We assume that this is an edge ef-

fect related to the finite aperture: the shot records near the edges ('half hyperbolas') contain less signal energy than the ones in the middle ('full hyperbolas'). It means that the receiver geometry compensates for this energy difference. Additionally, it can be observed that some undulations are present in the optimized received density (Figures 3c and 4c). This is the result of the transformation, at each iteration, from receiver density to acquisition geometry.

For the second study case we use the models shown in Figure 5. They contain flat layers with a high-velocity perturbation embedded in the first layer. The velocity of the perturbation is 2500 m/s for the first model (Figure 5a) and 4000 m/s for the second (Figure 5b). The sources are uniformly distributed every 100 m along the surface. The initial receiver geometry consists of $n_d = 41$ receivers located uniformly along the acquisition surface (Figure 6a). First, for the model in Figure 5a, we run the optimization algorithm for 30 iterations and obtain the receiver density shown in Figure 6c and the corresponding receiver geometry (Figure 6d).

The result of the optimization shows that the receiver density (Figure 6c) has higher values in the central part, meaning that the receivers have been relocated from the edges towards the center of the model (Figure 6d). This must be the result of the high-velocity perturbation, as apparently more data is needed in the center than at the edges to obtain a good image quality, given that the rest of the model is laterally homogeneous. It is interesting to notice that this effect apparently overrules the edge effects that showed up in the previous example. The experiment is now repeated for the model in Figure 5b with the higher velocity of the perturbation. It

is expected that now even more receivers are needed in the center part of the model. The comparison of the results is shown in Figure 7.

From Figure 7a, it can be seen that the optimized receiver density for model B is higher at the center than at the edges, with a shape that is indeed more pronounced than the one for model A. Therefore, the corresponding acquisition geometry (Figure 7b) for model B has more receivers located at the center than the optimized geometry for model A. From these two results we observe that a more complex subsurface leads to a higher imprint in the optimized acquisition geometry for the best imaging result.

To evaluate the quality of the optimized receiver geometry, we compare the imaging results from two experiments with the model in Figure 5b. In the first experiment, FWM is performed with the initial acquisition geometry shown in Figure 6a, leading to the image in Figure 8a. In the second experiment, FWM is performed with the optimized geometry (Figure 6d). The corresponding image is shown in Figure 8b. To compare the quality of the images, we plot their amplitude difference with respect to the reference image (Figures 8c and 8d). Figure 8e shows the comparison between the target functions when using the initial and optimized geometries.

Figure 8c shows a large amplitude difference with respect to the reference model compared to Figure 8d. Therefore, it becomes clear that the optimized geometry with more receivers located at the center, allows better imaging of the velocity perturbation. The comparison of the target functions (Figure 8e) shows that there is an improvement in the quality of the final image when using the optimized geometry (red curve).

The third model contains a salt dome embedded in a horizontally layered medium (Figure 9). We assume a scenario in which, due to the survey constraints, the sources can only be located at the right hand side of the model in the range from $x = 1450$ m to $x = 2450$ m. The sources are uniformly distributed and their spacing is 100 m.

To test the performance of the algorithm, we set up an acquisition geometry with $n_d = 25$ receivers, all being located at the left-hand side (Figure 10a). Our focus is to obtain a good image of the salt overhang, an area that could be of economic interest. Given the source distribution and the geometry of the model, there are no primary reflections related to the salt overhang that can be recorded by the receivers for any acquisition aperture. Therefore, imaging this section with primaries is not feasible. Nonetheless, FWM can make use of internal multiples for this purpose. These internal multiple reflections are generated between the lower horizontal reflector and the salt overhang and reflected towards the right hand side of the model (see red arrows in Figure 9). This indicates that the data needed for imaging the salt overhang should be recorded in this area. For this reason, the chosen initial acquisition geometry is far from ideal for this example, but we use it to test the performance of the algorithm. We run 20 iterations of the algorithm and plot the resulting receiver density and corresponding acquisition geometry in Figure 10d.

Figure 10c shows the optimized receiver density with an increasing tendency from left to right. As mentioned, due to the geometry of the model and the source distribution, the internal multiples generated by the salt overhang are reflected towards the right-hand side of the model (red arrows in Figure 9). For this reason, the al-

gorithm tends to increase the receiver density in this part of the model. Therefore, the corresponding acquisition geometry (Figure 10d) has more receivers in the right hand side.

To evaluate the quality of the optimized receiver geometry, we again compare the imaging results from two experiments. In the first experiment, FWM is performed with the initial acquisition geometry shown in Figure 10a, leading to the image in Figure 11a. In the second experiment, FWM is performed with the optimized geometry (Figure 10d). The corresponding image is shown in Figure 11b.

From the results in Figure 11, it can be seen that when the receivers are located at the left-hand side, no part of the salt dome is imaged. Only a few sections of the flat reflectors are visible. This is the result of the absence of multiple reflections in the recorded data, as these waves propagate towards the right-hand side where no receivers are present. This is not the case with the optimized geometry, and the flank of the salt is indeed imaged. The target function, shown in Figure 11c as a function of the iteration number, illustrates this huge difference.

Finally, in a more realistic scenario, we set up a uniform initial receiver geometry. The initial geometry and receiver density as well as the optimized results are shown in Figure 12.

From Figure 12 it can be seen that even by having a uniform initial geometry, the optimized result is similar to the one obtained in Figure 10. Therefore, the receivers are relocated mostly to the right hand side. We compare again the imaging results obtained with the initial and optimized geometries. The results are shown in Figure

13.

Figure 13a shows the FWM image obtained when the initial, uniform geometry (Figure 12a) is used and Figure 13b the image when the optimized geometry (Figure 12d) is used. The two results are rather similar, but not identical. Their difference (Figure 13c) shows that there is somewhat more energy present at the flanks of the salt dome in the optimized case. This occurs as more receivers are present in the right-hand side which allows to record more energy from the multiple reflections that illuminate the salt dome from below. This additional illumination is used by FWM to produce the improved image. The normalized target function (J_R), plotted versus iteration number in Figure 13d, shows that the target function is indeed minimized more when using the optimized geometry than when using the uniform one.

DISCUSSION

We have proposed an algorithm that optimizes the acquisition geometry for a particular subsurface model. Such a-priori knowledge on the subsurface could be obtained from legacy surveys. Also in the case of 4D seismics, such knowledge would be available. The results show that an optimized geometry may differ greatly from an initial - e.g., uniform - geometry.

As mentioned, the best seismic image of the subsurface would be obtained from fully sampled data, i.e., data that satisfies the Nyquist-Shannon sampling theorem. However, in practice this is impossible due to the associated high costs and other constraints. Therefore, a survey design methodology has to deal with a reduced

number of sources/receivers, which inevitably leads to a reduced image quality. For example, in the case of a geometry with a reduced number of receivers, the particular data carrying the information that allows to image certain part(s) of the subsurface may not be recorded. Our method aims to compensate this deficiency by increasing the receiver density in the zones where more data is needed (while reducing this density in other zones). This phenomenon could be clearly observed in our second example, where the receivers moved towards the center of the aperture to obtain a better image of the velocity perturbation. Here it was also observed that as the velocity of the perturbation became higher, the receiver geometry was adjusted even more.

In this research we focused on the signal of the scattered wavefields in the subsurface. The examples included in this paper are noise-free. However, in practice, noise is a critical issue to be handled in acquisition design. In the case of noisy data a number of receivers higher than initial proposed, may be required to achieve a certain image quality.

In our iterative scheme, the updates to the receiver density are computed by minimizing the misfit between a reference reflectivity image obtained from a fully sampled geometry and the reflectivity image obtained from the geometry being optimized. Our method could be modified to favour specific zones in the subsurface (target oriented) rather than the full subsurface. This is part of our ongoing work.

In this paper we chose a parameterization for the receiver geometry that allows to determine the location of individual receivers. In practice these could for instance

be the locations of nodal receivers at the water bottom.

Currently our implementation is still in 2D, but extension to 3D is required to make it practical. Similarly, while we focused on the receiver geometry only, also the source geometry could be considered. E.g., during the odd iterations the receiver geometry could be updated while during the even iterations the source geometry could be updated in the same optimization scheme. Because of the symmetry of sources and receivers, the procedure for optimizing the source density function is identical to the one for the receiver side.

CONCLUSION

From the results of this research we conclude that a survey design can be adjusted to a particular subsurface when a-priori knowledge of that subsurface is available. This makes it possible to design the acquisition geometry of a (next) seismic survey for optimum imaging.

We recognize the importance of experimental survey design by means of modeling and manual adjustment of the acquisition geometry. However, we believe that a deterministic optimization of the acquisition geometry, such as the one presented in this paper, could best exploit the content of the available subsurface information. As full-wavefield migration is used as the imaging algorithm, the use of multiples for imaging is taken into account in the survey design.

The examples presented in this paper show the influence of the subsurface on the

acquisition geometry, resulting in optimum, non-uniform receiver density functions. Increasing the subsurface complexity increases the non-uniformity of the receiver distribution.

ACKNOWLEDGMENTS

The authors thank the sponsors of the Delphi Consortium for their support.

APPENDIX A

DERIVATION OF THE UPDATE DIRECTION

We repeat equation 20 being the derivative of target function $J_{R,i}$ with respect to the receiver density $\mathbf{\Phi}$:

$$\frac{\partial J_{R,i}}{\partial \mathbf{\Phi}} = \frac{\partial}{\partial \mathbf{\Phi}} \left[\sum_n \|\Delta \mathbf{R}_i(z_n)\|^2 \right]. \tag{A-1}$$

This expression can be written as:

$$\frac{\partial J_{R,i}}{\partial \mathbf{\Phi}} = 2 \sum_n \left[\Delta \mathbf{R}_i(z_n) \frac{\partial \Delta \mathbf{R}_i(z_n)}{\partial \mathbf{\Phi}} \right]. \tag{A-2}$$

Using equation 16, the term $\Delta \mathbf{R}(z_n)$ can be written as:

$$\Delta \mathbf{R}_i(z_n) = \mathbf{R}(z_n) - \mathbf{R}_i(z_n) - \alpha_i \delta \mathbf{R}_i(z_n). \tag{A-3}$$

From equation 18b it follows that $\Delta \mathbf{R}_{i-1}(z_n) = \mathbf{R}(z_n) - \mathbf{R}_i(z_n)$. By substituting this in equation A-3 we obtain:

$$\Delta \mathbf{R}_i(z_n) = \Delta \mathbf{R}_{i-1}(z_n) - \alpha_i \delta \mathbf{R}_i(z_n). \tag{A-4}$$

Therefore, the derivative term in the right hand side of equation A-2 can be written as:

$$\frac{\partial \Delta \mathbf{R}_i(z_n)}{\partial \mathbf{\Phi}} = \frac{\partial}{\partial \mathbf{\Phi}} \left[\Delta \mathbf{R}_{i-1}(z_n) - \alpha_i \delta \mathbf{R}_i(z_n) \right]. \tag{A-5}$$

Next, we express the reflectivity update direction $\delta \mathbf{R}_i(z_n)$ in terms of receiver density $\mathbf{\Phi}$. To do this, we substitute equation 12 in equation A-5

$$\frac{\partial \Delta \mathbf{R}_i(z_n)}{\partial \mathbf{\Phi}} = \frac{\partial}{\partial \mathbf{\Phi}} \Bigg\{ \Delta \mathbf{R}_{i-1}(z_n) - \alpha_i [\mathbf{H}_i(x, z_n)]^{-1} \left[\delta \overline{\mathbf{R}}_i^{\cup}(z_n) + \delta \overline{\mathbf{R}}_i^{\cap}(z_n) \right] \Bigg\}. \tag{A-6}$$

Subsequently we apply equations 9a and 9b and assume angle-independent reflectivity, see equations 11a and 11b:

$$\begin{aligned} \frac{\partial \Delta \mathbf{R}_i(z_n)}{\partial \mathbf{\Phi}} = \frac{\partial}{\partial \mathbf{\Phi}} \Bigg\{ & \Delta \mathbf{R}_{i-1}(z_n) \\ & - \alpha_i |f|^2 \left[\mathbf{H}_i(x, z_n) \right]^{-1} \sum_{\omega} \Big[\left[\mathbf{U}_i^{-}(z_0; z_n) \right]^H \Delta \mathbf{P}_i(z_0, z_0) \left[\mathbf{X}_i^{+}(z_n, z_0) \right]^H \\ & + \left[\mathbf{U}_i^{\cup}(z_0, z_n) \right]^H \Delta \mathbf{P}_i(z_0, z_0) \left[\mathbf{X}_{i-1}^{-}(z_n, z_0) \right]^H \Big] \Bigg\}. \end{aligned} \tag{A-7}$$

To move along the direction of steepest descent, finite, real-valued updates are needed for the acquisition geometry. Therefore, instead of using the receiver matrix $\mathbf{D}_i(z_0)$, we use the receiver density matrix $\mathbf{\Phi}_i(z_0)$ in equation 8a, which then becomes:

$$\Delta \mathbf{P}_i(z_0, z_0) = \mathbf{\Phi}_i(z_0) \Delta \mathbf{X}_i^{-}(z_0, z_0), \tag{A-8}$$

Consequently, we substitute equation A-8 in equation A-7 and obtain:

$$\begin{aligned} \frac{\partial \Delta \mathbf{R}_i(z_n)}{\partial \mathbf{\Phi}} = \frac{\partial}{\partial \mathbf{\Phi}} \Bigg\{ & \Delta \mathbf{R}_{i-1}(z_n) \\ & - \alpha_i |f|^2 \left[\mathbf{H}_i(x, z_n) \right]^{-1} \sum_{\omega} \Big[\left[\mathbf{U}_i^{-}(z_0, z_n) \right]^H \mathbf{\Phi}_i(z_0) \Delta \mathbf{X}_i^{-}(z_0, z_0) \left[\mathbf{X}_i^{+}(z_n, z_0) \right]^H \\ & + \left[\mathbf{U}_i^{\cup}(z_0, z_n) \right]^H \mathbf{\Phi}_i(z_0) \Delta \mathbf{X}_i^{-}(z_0, z_0) \left[\mathbf{X}_{i-1}^{-}(z_n, z_0) \right]^H \Big] \Bigg\}. \end{aligned} \tag{A-9}$$

The differentiation with respect to $\mathbf{\Phi}$ in equation A-9 gives as result:

$$\frac{\partial \Delta \mathbf{R}_i(z_n)}{\partial \mathbf{\Phi}} = -\alpha_i |f|^2 \left[\mathbf{H}_i(x, z_n)\right]^{-1} \sum_{\omega} \big[\mathbf{U}_i^{-}(z_0, z_n)\mathbf{X}_i^{+}(z_n, z_0) + \mathbf{U}_i^{\cup}(z_0, z_n)\mathbf{X}_{i-1}^{-}(z_n, z_0)\big] \left[\Delta \mathbf{X}_i^{-}(z_0, z_0)\right]^H. \quad \text{(A-10)}$$

Finally, by substituting equation A-10 in equation A-2 we obtain:

$$\frac{\partial J_{R,i}}{\partial \mathbf{\Phi}} = \sum_n \sum_{\omega} -2\alpha_i |f|^2 \left[\mathbf{H}_i(x, z_n)\right]^{-1} \Big\{\mathbf{U}_i^{-}(z_0, z_n)\Delta \mathbf{R}_i(z_n)\mathbf{X}_i^{+}(z_n, z_0) + \mathbf{U}_i^{\cup}(z_0, z_n)\Delta \mathbf{R}_i(z_n)\mathbf{X}_{i-1}^{-}(z_n, z_0)\Big\}[\Delta \mathbf{X}_i^{-}(z_0, z_0)]^H. \quad \text{(A-11)}$$

The term between braces in equation A-11 is a modeled wavefield based on the residual reflectivity image $\Delta \mathbf{R}_i(z_n)$. Therefore, we replace this term with $\Delta \mathbf{P}_r(\Delta \mathbf{R}_i(z_n))$ (See equation 15). Consequently, the update direction can be expressed as:

$$\frac{\partial J_{R,i}}{\partial \mathbf{\Phi}} = \sum_n \sum_{\omega} -2\alpha_i |f|^2 \left[\mathbf{H}_i(x, z_n)\right]^{-1} \Delta \mathbf{P}_r(\Delta \mathbf{R}_i(z_n))[\Delta \mathbf{X}_i^{-}(z_0, z_0)]^H. \quad \text{(A-12)}$$

Equation A-12 contains the correlation between the data residual $\Delta \mathbf{X}_i^{-}$ and the wavefield $\Delta \mathbf{P}_r$ modeled from the residual reflectivity image $\Delta \mathbf{R}_i$. Therefore, it can be interpreted as a mapping from the model update to the data space, at the sampling locations where more data is needed. Finally, the update direction is given by:

$$\delta \mathbf{\Phi}_i = -\frac{\partial J_{R,i}^*}{\partial \mathbf{\Phi}}. \quad \text{(A-13)}$$

APPENDIX B

DERIVATION OF THE SCALING PARAMETER

In the gradient descent scheme, the optimal scaling parameter is found when the update direction at iteration $i+1$, is orthogonal to the direction at iteration i (Shewchuk, 1994). Therefore, the following condition must hold:

$$[\delta\mathbf{\Phi}_{i+1}]^H \delta\mathbf{\Phi}_i = 0. \tag{B-1}$$

To find the update direction $\delta\mathbf{\Phi}_{i+1}$, we use equation A-12 and assume that the term $\mathbf{\Phi}$, which is implicitly contained, can be linearized.

$$\delta\mathbf{\Phi}_{i+1} = \sum_n \sum_\omega -2\alpha_i |f|^2 \left[\mathbf{H}_i(x, z_n)\right]^{-1} \left[\Delta\mathbf{P}_r(\Delta\mathbf{R}_i(z_n))\right]_{\mathbf{\Phi}} \left[\Delta\mathbf{X}_i^-(z_0, z_0)\right]^H. \tag{B-2}$$

The subscript $\mathbf{\Phi}$ in this and subsequent equations, makes reference to the variables computed for finding the optimal scaling parameter. This means, in the direction of $\delta\mathbf{\Phi}_{i+1}$. The wavefield $[\Delta\mathbf{P}_r(\Delta\mathbf{R}_i(z_n))]_{\mathbf{\Phi}}$ is therefore:

$$\begin{aligned}[\Delta\mathbf{P}_r(\Delta\mathbf{R}_i(z_n))]_{\mathbf{\Phi}} &= \mathbf{U}_i^-(z_0, z_n)[\Delta\mathbf{R}_i(z_n)]_{\mathbf{\Phi}}\mathbf{X}_i^+(z_n, z_0) \\ &+ \mathbf{U}_i^{\cup}(z_0, z_n)[\Delta\mathbf{R}_i(z_n)]_{\mathbf{\Phi}}\mathbf{X}_{i-1}^-(z_n, z_0),\end{aligned} \tag{B-3}$$

where $[\Delta\mathbf{R}_i(z_n)]_{\mathbf{\Phi}}$ is:

$$\begin{aligned}[\Delta\mathbf{R}_i(z_n)]_{\mathbf{\Phi}} &= \Delta\mathbf{R}_{i-1}(z_n) \\ -\alpha_i |f|^2 \left[\mathbf{H}_i(x, z_n)\right]^{-1} \sum_\omega \Big\{ &\left[\mathbf{U}_i^-(z_0, z_n)\right]^H \mathbf{\Phi}_{i+1} \Delta\mathbf{X}_i^-(z_0, z_0) \left[\mathbf{X}_i^+(z_n, z_0)\right]^H \\ &+ \left[\mathbf{U}_i^{\cup}(z_0, z_n)\right]^H \mathbf{\Phi}_{i+1} \Delta\mathbf{X}_i^-(z_0, z_0) \left[\mathbf{X}_{i-1}^-(z_n, z_0)\right]^H \Big\}.\end{aligned} \tag{B-4}$$

In equation B-4, the receiver density $\mathbf{\Phi}_{i+1}$ is used instead of $\mathbf{\Phi}_i$. Therefore, we may substitute equation 19 in equation B-4:

$$
\begin{aligned}
&[\Delta\mathbf{R}_i(z_n)]_{\mathbf{\Phi}} = \Delta\mathbf{R}_{i-1}(z_n) \\
&-\alpha_i|f|^2\left[\mathbf{H}_i(x,z_n)\right]^{-1}\sum_{\omega}\Big\{\left[\mathbf{U}_i^{-}(z_0,z_n)\right]^H(\mathbf{\Phi}_i+\beta_i\delta\mathbf{\Phi}_i)\Delta\mathbf{X}_i^{-}(z_0,z_0)\left[\mathbf{X}_i^{+}(z_n,z_0)\right]^H \\
&\qquad\qquad +\left[\mathbf{U}_i^{\cup}(z_0,z_n)\right]^H(\mathbf{\Phi}_i+\beta_i\delta\mathbf{\Phi}_i)\Delta\mathbf{X}_i^{-}(z_0,z_0)\left[\mathbf{X}_{i-1}^{-}(z_n,z_0)\right]^H\Big\}.
\end{aligned}
\tag{B-5}
$$

By substituting equation B-5 in equation B-3, and substituting the result in equation B-2 we obtain:

$$
\delta\mathbf{\Phi}_{i+1} = \delta\mathbf{\Phi}_i + \beta_i\sum_n\sum_{\omega} -2\alpha_i|f|^2\left[\mathbf{H}_i(x,z_n)\right]^{-1}\Delta\mathbf{P}_r(\mathbf{R}_\phi(z_n))[\Delta\mathbf{X}_i^{-}(z_0,z_0)]^H, \tag{B-6}
$$

where $\mathbf{R}_\phi(z_n)$ is an image obtained from:

$$
\begin{aligned}
\mathbf{R}_\phi(z_n) = \sum_{\omega}\Big\{&\left[\mathbf{U}_i^{-}(z_0,z_n)\right]^H\delta\mathbf{\Phi}_i\Delta\mathbf{X}_i^{-}(z_0,z_0)\left[\mathbf{X}_i^{+}(z_n,z_0)\right]^H. \\
&+\left[\mathbf{U}_i^{\cup}(z_0,z_n)\right]^H\delta\mathbf{\Phi}_i\Delta\mathbf{X}_i^{-}(z_0,z_0)\left[\mathbf{X}_{i-1}^{-}(z_n,z_0)\right]^H\Big\}.
\end{aligned}
\tag{B-7}
$$

Finally, by substituting equation B-6 in equation B-1, we obtain the optimal scaling parameter:

$$
\beta_i = \frac{(\delta\mathbf{\Phi}_i)^H\delta\mathbf{\Phi}_i}{\left[-2\alpha_i|f|^2\left[\mathbf{H}_i(x,z_n)\right]^{-1}\Delta\mathbf{P}_r(\mathbf{R}_\phi(z_n))[\Delta\mathbf{X}_i^{-}(z_0,z_0)]^H\right]^H\delta\mathbf{\Phi}_i}. \tag{B-8}
$$

From equation B-8, the denominator can be computed via the following steps:

1. Compute the reflectivity image $\mathbf{R}_\phi(z_n)$
2. From this image, model seismic data $\Delta\mathbf{P}_r(\mathbf{R}_\phi(z_n))$
3. Correlate this data with the data residual $\Delta\mathbf{X}_i^{-}(z_0,z_0)$.
4. Correlate this result with the current update direction $\delta\mathbf{\Phi}_i$.

REFERENCES

Alerini, M., B. Traub, C. Ravaut, and E. Duveneck, 2009, Prestack depth imaging of ocean-bottom node data: GEOPHYSICS, **74**, WCA57–WCA63; doi: 10.1190/1.3204767.

Berkhout, A. G., 2014a, Review Paper: An outlook on the future of seismic imaging, Part I: forward and reverse modelling: Geophysical Prospecting, **62**, 911–930; doi: 10.1111/1365-2478.12161. (_eprint: https://onlinelibrary.wiley.com/doi/pdf/10.1111/1365-2478.12161).

———, 2014b, Review Paper: An outlook on the future of seismic imaging, Part II: Full-Wavefield Migration: An outlook on the future of seismic imaging, Part II: Geophysical Prospecting, **62**, 931–949; doi: 10.1111/1365-2478.12154.

Berkhout, A. J., 1982, Seismic migration, imaging of acoustic energy by wave field extrapolation, A. theoretical aspects: Elsevier.

Berkhout, A. J., L. Ongkiehong, A. W. F. Volker, and G. Blacquière, 2001, Comprehensive assessment of seismic acquisition geometries by focal beams - Part I: Theoretical considerations: Geophysics, **66**, 911–917.

Davydenko, M., and D. J. Verschuur, 2017, Full-wavefield migration: using surface and internal multiples in imaging: Geophys. Prosp., **65**, 7–21.

———, 2018, Including and using internal multiples in closed-loop imaging — Field data examples: GEOPHYSICS, **83**, R297–R305; doi: 10.1190/geo2017-0533.1.

Lloyd, S., 1982, Least squares quantization in PCM: IEEE Transactions on Information Theory, **28**, 129–137; doi: 10.1109/TIT.1982.1056489.

Maurer, H., A. Curtis, and D. E. Boerner, 2010, Recent advances in optimized geophysical survey design: GEOPHYSICS, **75**, 75A177–75A194; doi: 10.1190/1.3484194.

Muerdter, D., and D. Ratcliff, 2001, Understanding subsalt illumination through ray-trace modeling, Part 1: Simple 2-D salt models: The Leading Edge, **20**, 578–595.

Nakayama, S., G. Blacquière, and T. Ishiyama, 2019, Automated survey design for blended acquisition with irregular spatial sampling via the integration of a meta-heuristic and deep learning: GEOPHYSICS, **84**, P47–P60; doi: 10.1190/geo2018-0826.1.

Regone, C. J., 2006, A modeling approach to wide-azimuth design for subsalt imaging: The Leading Edge, **25**, 1467–1475.

Revelo-Obando, B., and G. Blacquière, 2021, Acquisition geometry analysis with point-spread functions: Geophysical Prospecting, **69**, 1606–1624; doi: 10.1111/1365-2478.13128.

Secord, A., 2002, Weighted Voronoi Stippling: Proceedings of the 2nd International Symposium on Non-Photorealistic Animation and Rendering, Association for Computing Machinery, 37–43.

Shewchuk, J. R., 1994, An Introduction to the Conjugate Gradient Method Without the Agonizing Pain: Technical Report, Carnegie Mellon University, USA.

Singh, V., A. Venkataraman, R. Ho, E. Neumann, and B. Laugier, 2016, Ocean-bottom node acquisition optimization: SEG Technical Program Expanded Abstracts 2016, Society of Exploration Geophysicists, 193–197.

Staal, X., 2015, Combined imaging and velocity estimation by Joint Migration Inver-

sion: PhD thesis, Technische Universiteit Delft.

Theriot, C., M. McDonald, M. R. Kamarudin, and P. Yu, 2014, Survey design for optimized ocean bottom node acquisition: SEG Technical Program Expanded Abstracts 2014, Society of Exploration Geophysicists, 213–217.

Vermeer, G. J. O., 2012, 3D Seismic Survey Design, 2 ed.: Society of Exploration Geophysicists. Geophysical References Series, No. 2.

Volker, A. W. F., G. Blacquière, A. J. Berkhout, and L. Ongkiehong, 2001, Comprehensive assessment of seismic acquisition geometries by focal beams - Part II: Practical aspects and examples: Geophysics, **66**, 918–931.

Wu, S., D. J. Verschuur, and G. Blacquière, 2022, Automated Seismic Acquisition Geometry Design for Optimized Illumination at the Target: A Linearized Approach: IEEE Transactions on Geoscience and Remote Sensing, **60**, 1–13; doi: 10.1109/TGRS.2021.3131365.

LIST OF FIGURES

is higher. (a) Comparison of optimized receiver densities. (b) Comparison of optimized geometries.

8 Imaging up to 40 Hz of the model in Figure 5b with (a) initial and (b) optimized geometries. (c) Amplitude difference between (a) and reference model. (d) Amplitude difference between (b) and reference model. (e) Comparison of target functions.

9 Salt dome P-wave velocity model. The lower layer at $z = 1000$ m generates strong internal multiples towards the salt dome overhang. The red stars on the top indicate the position of the sources.

10 Optimized receiver geometry for the model in Figure 9. The receivers are located at the surface $z = 0$ m. After optimization, the receivers are re-located towards the right hand side of the model. (a) Initial receiver geometry, (b) initial receiver density, (c) optimized receiver density, (d) optimized receiver geometry.

11 Imaging the model in Figure 9. (a) Using the initial geometry in Figure 10a. (b) Using the optimized geometry in Figure 10d. (c) Comparison of target functions.

12 Optimized receiver geometry for the model in Figure 9. The receivers are located at the surface $z = 0$ m. After optimization, the receivers are re-located towards the right hand side of the model. (a) Initial receiver geometry, (b) initial receiver density, (c) optimized receiver density, (d) optimized receiver geometry.

13 Imaging the model in Figure 9. (a) Using the initial geometry in Figure 12a. (b) Using the optimized geometry in Figure 12d. (c) Amplitude difference between (a) and (b). (d) Comparison of target functions. The target function is always lower for the optimized geometry than for the uniform geometry.

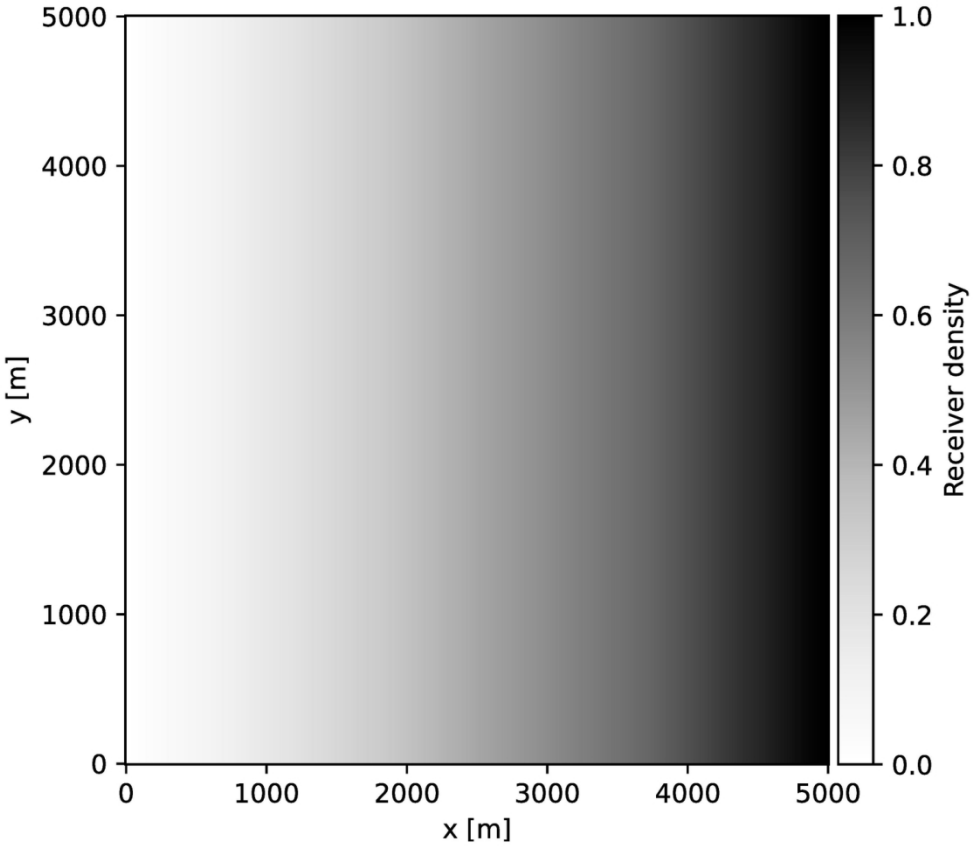

Figure 1a. (a) Receiver density. Linear increase in the x-direction. (b) Corresponding receiver geometry created through the transformation g for $n_d = 2500$. More receivers located in the right-hand side where the density is higher.

135x118mm (300 x 300 DPI)

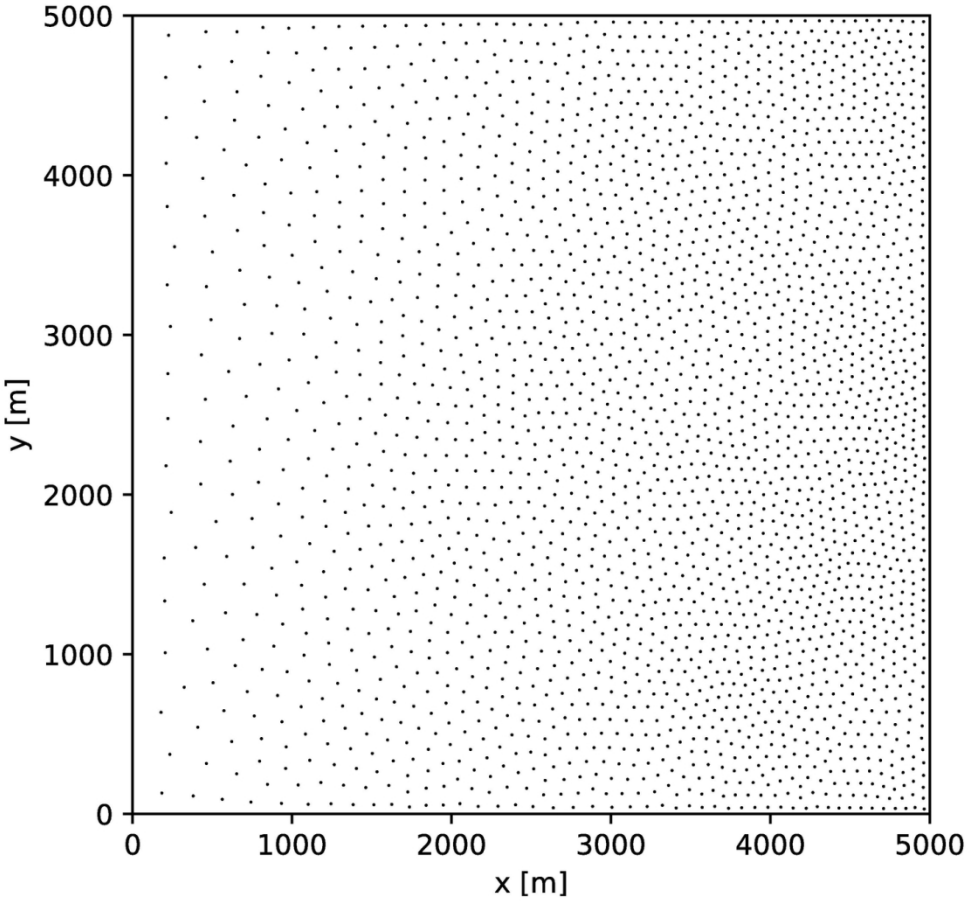

Figure 1b.(a) Receiver density. Linear increase in the x-direction. (b) Corresponding receiver geometry created through the transformation g for $n_d = 2500$. More receivers located in the right-hand side where the density is higher.

127x118mm (300 x 300 DPI)

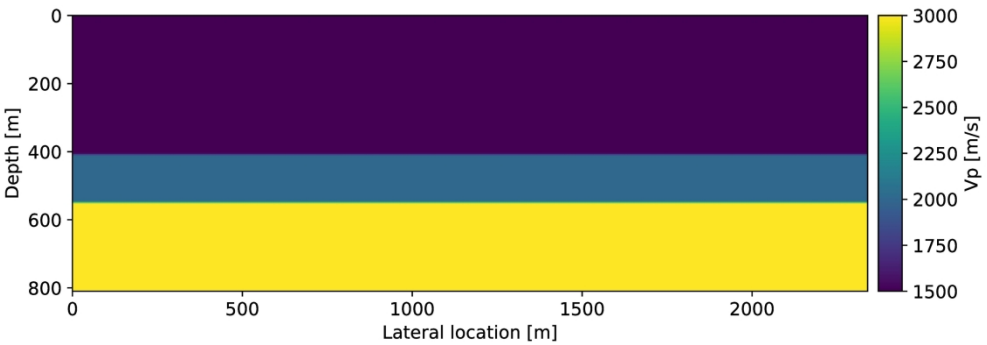

Figure 2. P-wave velocity model with three horizontal layers. The velocities of the layers from top to bottom are $Vp = 1500$ m/s, $ 2200$ m/s and 3000 m/s.

236x84mm (300 x 300 DPI)

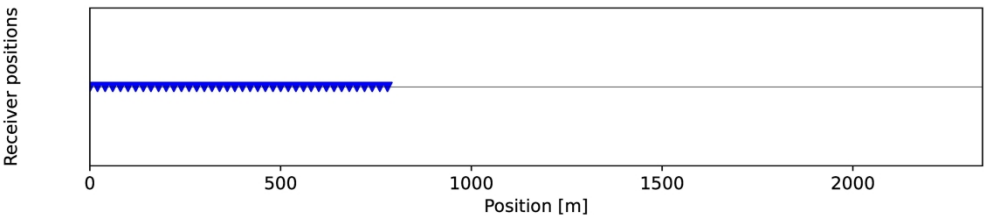

Figure 3a. Geometry optimization for the model in Figure~\ref{fig:Figure2_v}. The receivers are located at the surface $z=0$ m. (a) Initial receiver geometry, (b) initial receiver density, (c) optimized receiver density, (d) optimized receiver geometry.

242x57mm (300 x 300 DPI)

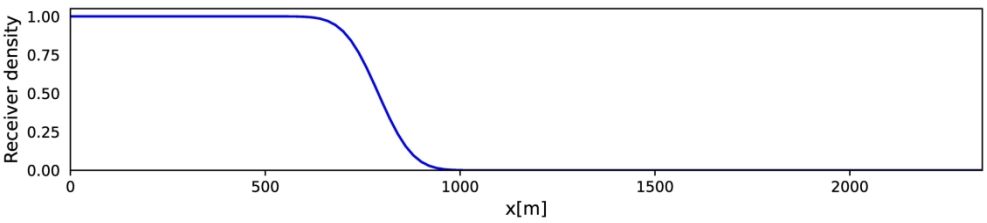

Figure 3b. Geometry optimization for the model in Figure~\ref{fig:Figure2_v}. The receivers are located at the surface $z=0$ m. (a) Initial receiver geometry, (b) initial receiver density, (c) optimized receiver density, (d) optimized receiver geometry.

237x54mm (300 x 300 DPI)

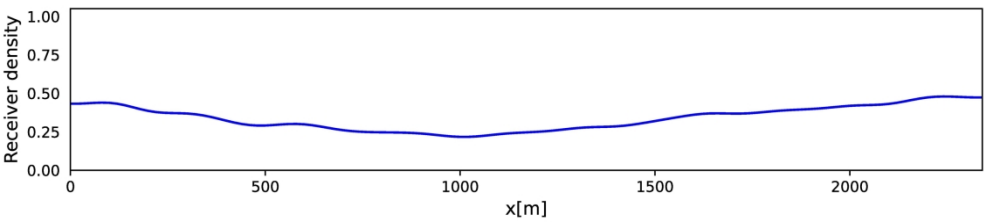

Figure 3c. Geometry optimization for the model in Figure~\ref{fig:Figure2_v}. The receivers are located at the surface $z=0$ m. (a) Initial receiver geometry, (b) initial receiver density, (c) optimized receiver density, (d) optimized receiver geometry.

237x54mm (300 x 300 DPI)

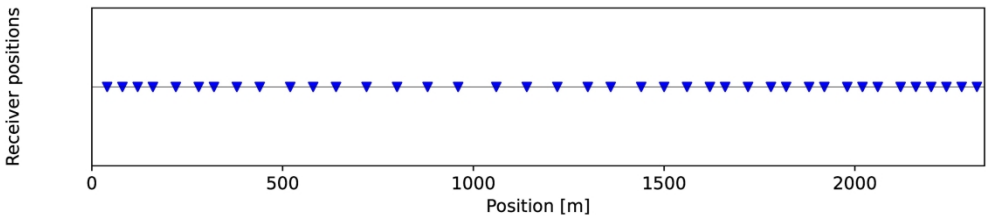

Figure 3d. Geometry optimization for the model in Figure~\ref{fig:Figure2_v}. The receivers are located at the surface $z=0$ m. (a) Initial receiver geometry, (b) initial receiver density, (c) optimized receiver density, (d) optimized receiver geometry.

242x57mm (300 x 300 DPI)

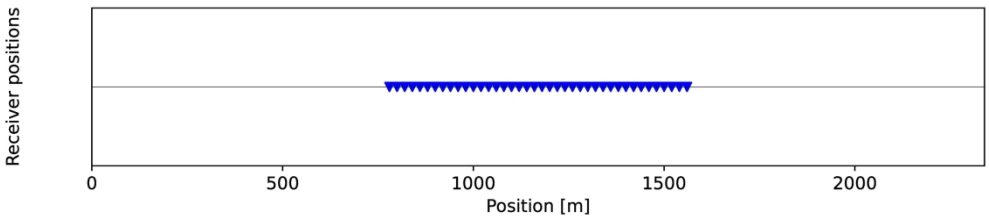

Figure 4a. Geometry optimization for the model in Figure~\ref{fig:Figure2_v}. The receivers are located at the surface $z=0$ m. (a) Initial receiver geometry, (b) initial receiver density, (c) optimized receiver density, (d) optimized receiver geometry.

242x57mm (300 x 300 DPI)

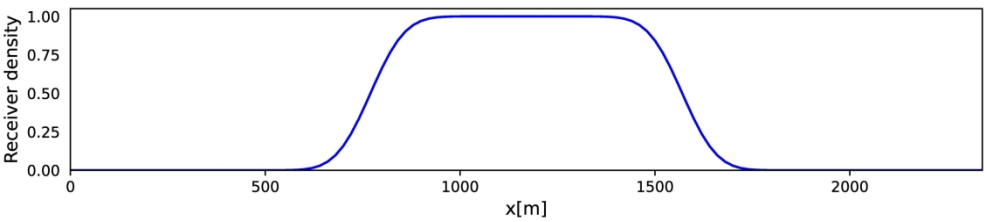

Figure 4b. Geometry optimization for the model in Figure~\ref{fig:Figure2_v}. The receivers are located at the surface $z=0$ m. (a) Initial receiver geometry, (b) initial receiver density, (c) optimized receiver density, (d) optimized receiver geometry.

237x54mm (300 x 300 DPI)

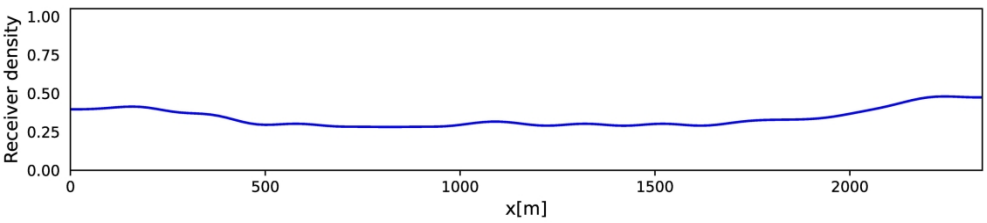

Figure 4c. Geometry optimization for the model in Figure~\ref{fig:Figure2_v}. The receivers are located at the surface $z=0$ m. (a) Initial receiver geometry, (b) initial receiver density, (c) optimized receiver density, (d) optimized receiver geometry.

237x54mm (300 x 300 DPI)

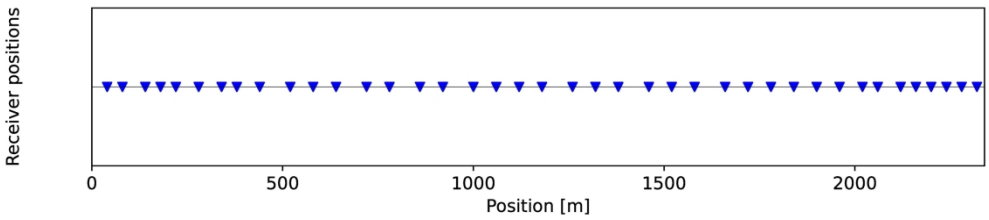

Figure 4d. Geometry optimization for the model in Figure~\ref{fig:Figure2_v}. The receivers are located at the surface $z=0$ m. (a) Initial receiver geometry, (b) initial receiver density, (c) optimized receiver density, (d) optimized receiver geometry.

242x57mm (300 x 300 DPI)

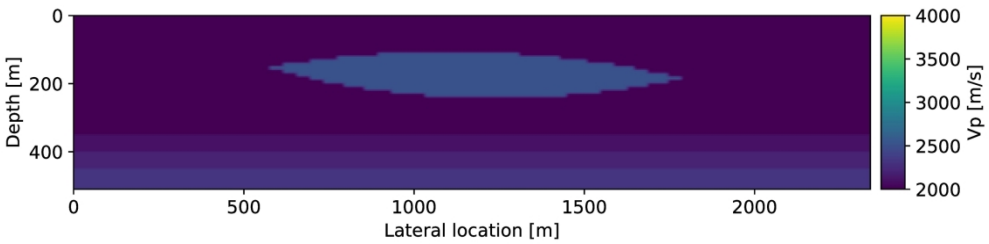

Figure 5a. Horizontally layered P-wave velocity models with high-velocity perturbation embedded in the first layer. (a) Model A: perturbation with v = 2500 m/s. (b) Model B: perturbation with v = 4000 m/s.

236x59mm (300 x 300 DPI)

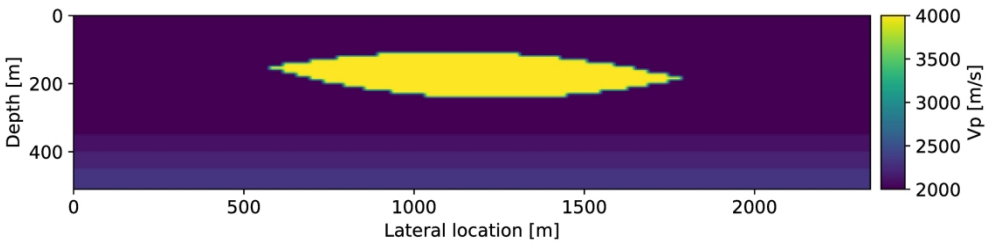

Figure 5b. Horizontally layered P-wave velocity models with high-velocity perturbation embedded in the first layer. (a) Model A: perturbation with v = 2500 m/s. (b) Model B: perturbation with v = 4000 m/s.

236x59mm (300 x 300 DPI)

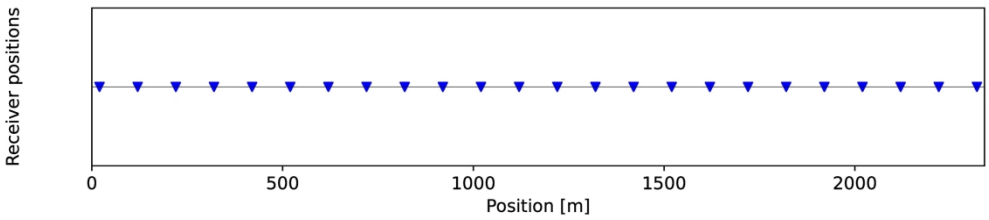

Figure 6a. Initial and optimized receiver geometries for the model in Figure \ref{fig:Figure5A_v}. The receivers are located at the surface $z=0$ m. The optimized geometry shows that more receivers are needed above the high-velocity perturbation in order to obtain a better image. (a) Initial receiver geometry, (b) initial receiver density, (c) optimized receiver density, (d) optimized receiver geometry.

242x57mm (300 x 300 DPI)

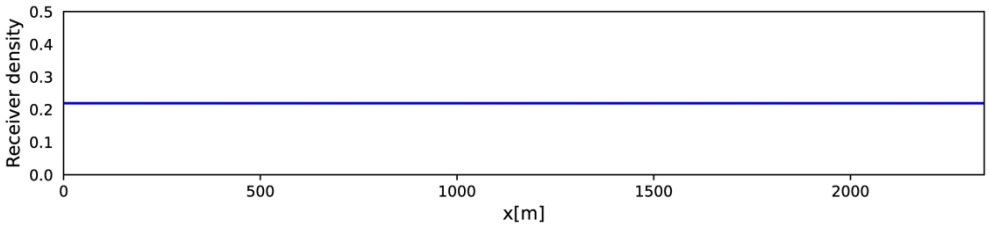

Figure 6b. Initial and optimized receiver geometries for the model in Figure \ref{fig:Figure5A_v}. The receivers are located at the surface $z=0$ m. The optimized geometry shows that more receivers are needed above the high-velocity perturbation in order to obtain a better image. (a) Initial receiver geometry, (b) initial receiver density, (c) optimized receiver density, (d) optimized receiver geometry.

235x56mm (300 x 300 DPI)

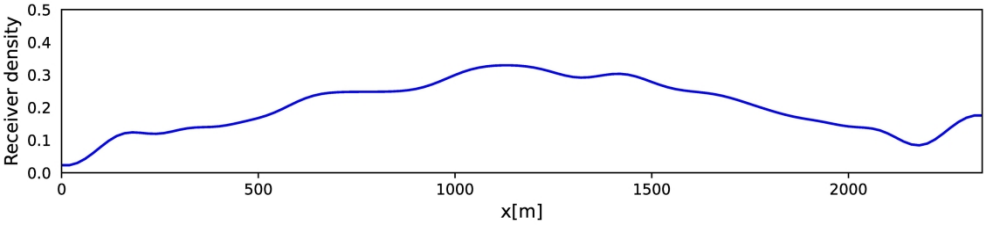

Figure 6c. Initial and optimized receiver geometries for the model in Figure \ref{fig:Figure5A_v}. The receivers are located at the surface $z=0$ m. The optimized geometry shows that more receivers are needed above the high-velocity perturbation in order to obtain a better image. (a) Initial receiver geometry, (b) initial receiver density, (c) optimized receiver density, (d) optimized receiver geometry.

235x56mm (300 x 300 DPI)

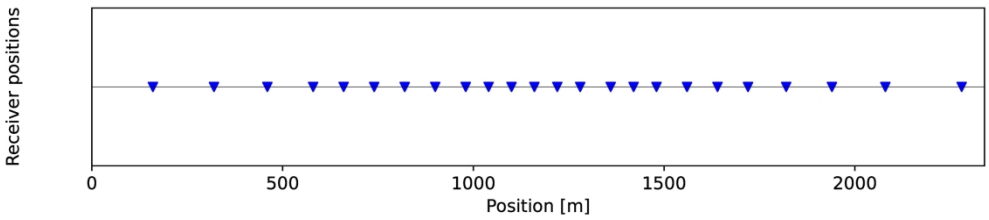

Figure 6d. Initial and optimized receiver geometries for the model in Figure \ref{fig:Figure5A_v}. The receivers are located at the surface $z=0$ m. The optimized geometry shows that more receivers are needed above the high-velocity perturbation in order to obtain a better image. (a) Initial receiver geometry, (b) initial receiver density, (c) optimized receiver density, (d) optimized receiver geometry.

242x57mm (300 x 300 DPI)

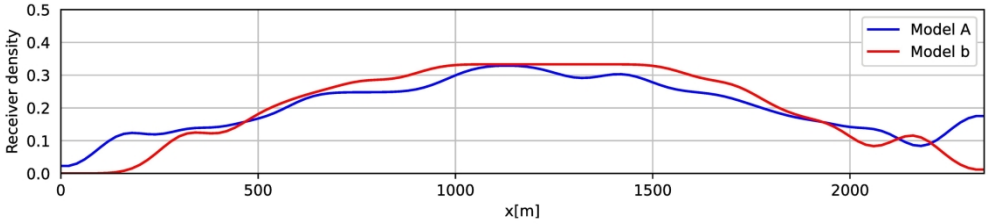

Figure 7a. Comparison of optimized geometries for models A (Figure \ref{fig:Figure5A_v}) and B (Figure \ref{fig:Figure5B_v}). More receivers are located at the center for model B as the velocity perturbation is higher. (a) Comparison of optimized receiver densities. (b) Comparison of optimized geometries.

234x55mm (300 x 300 DPI)

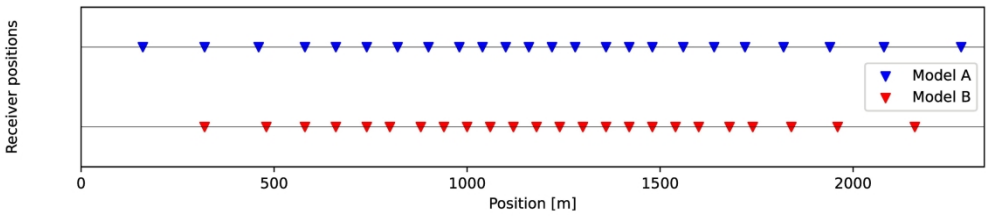

Figure 7b. Comparison of optimized geometries for models A (Figure \ref{fig:Figure5A_v}) and B (Figure \ref{fig:Figure5B_v}). More receivers are located at the center for model B as the velocity perturbation is higher. (a) Comparison of optimized receiver densities. (b) Comparison of optimized geometries.

239x55mm (300 x 300 DPI)

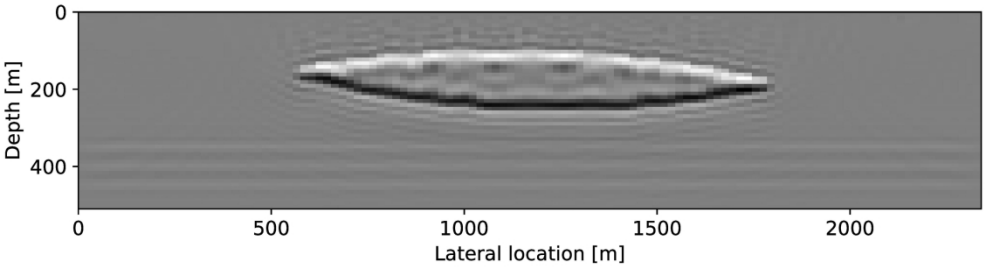

Figure 8a. Imaging up to 40 Hz of the model in Figure \ref{fig:Figure5B_v} with (a) initial and (b) optimized geometries. (c) Amplitude difference between (a) and reference model. (d) Amplitude difference between (b) and reference model. (e) Comparison of target functions.

217x61mm (300 x 300 DPI)

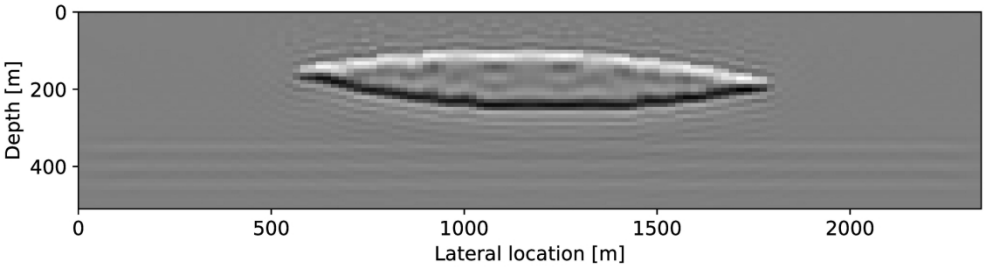

Figure 8b. Imaging up to 40 Hz of the model in Figure \ref{fig:Figure5B_v} with (a) initial and (b) optimized geometries. (c) Amplitude difference between (a) and reference model. (d) Amplitude difference between (b) and reference model. (e) Comparison of target functions.

217x61mm (300 x 300 DPI)

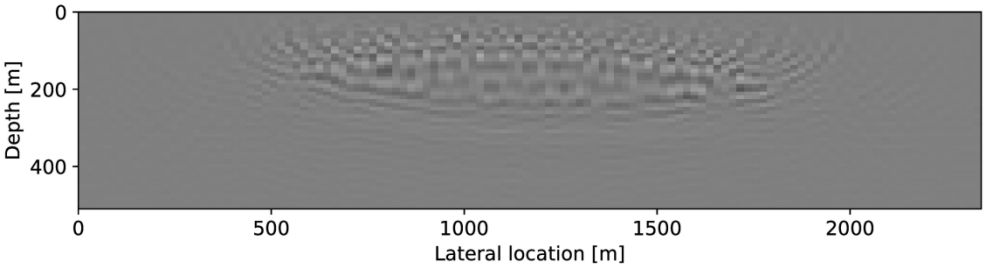

Figure 8c. Imaging up to 40 Hz of the model in Figure \ref{fig:Figure5B_v} with (a) initial and (b) optimized geometries. (c) Amplitude difference between (a) and reference model. (d) Amplitude difference between (b) and reference model. (e) Comparison of target functions.

217x61mm (300 x 300 DPI)

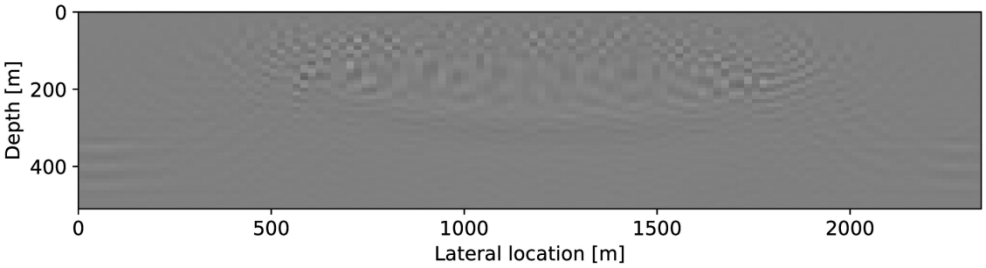

Figure 8d. Imaging up to 40 Hz of the model in Figure \ref{fig:Figure5B_v} with (a) initial and (b) optimized geometries. (c) Amplitude difference between (a) and reference model. (d) Amplitude difference between (b) and reference model. (e) Comparison of target functions.

217x61mm (300 x 300 DPI)

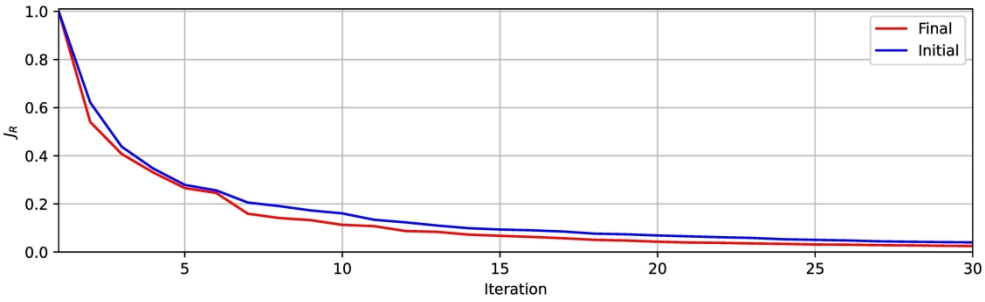

Figure 8e. Imaging up to 40 Hz of the model in Figure \ref{fig:Figure5B_v} with (a) initial and (b) optimized geometries. (c) Amplitude difference between (a) and reference model. (d) Amplitude difference between (b) and reference model. (e) Comparison of target functions.

236x74mm (300 x 300 DPI)

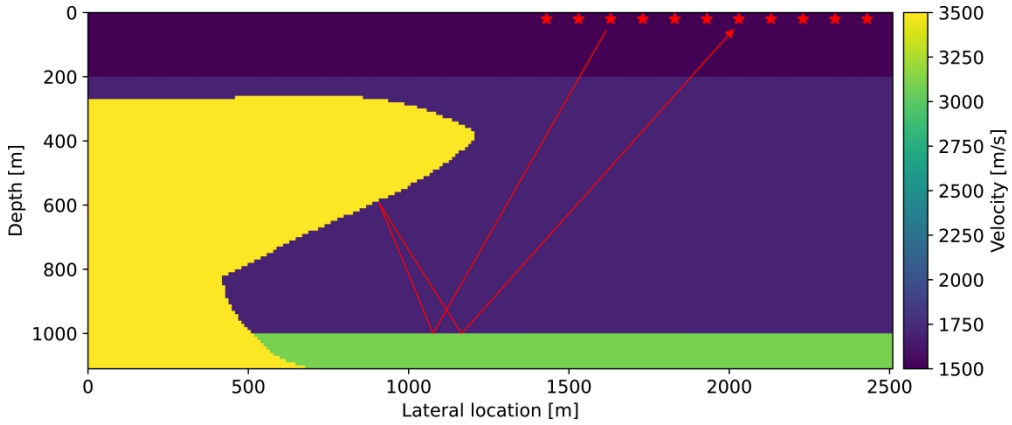

Figure 9. Salt dome P-wave velocity model. The lower layer at $z = 1000$ m generates strong internal multiples towards the salt dome overhang. The red stars on the top indicate the position of the sources.

805x332mm (600 x 600 DPI)

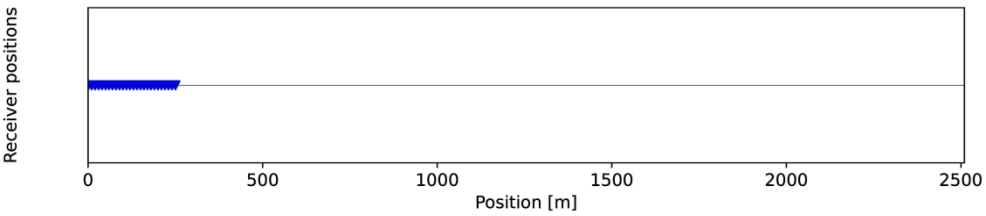

Figure 10a. Optimized receiver geometry for the model in Figure \ref{fig:Figure9_v}. The receivers are located at the surface $z=0$ m. After optimization, the receivers are re-located towards the right hand side of the model. (a) Initial receiver geometry, (b) initial receiver density, (c) optimized receiver density, (d) optimized receiver geometry.

246x57mm (300 x 300 DPI)

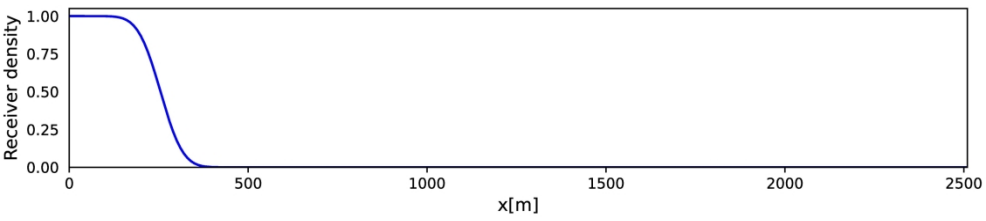

Figure 10b. Optimized receiver geometry for the model in Figure \ref{fig:Figure9_v}. The receivers are located at the surface $z=0$ m. After optimization, the receivers are re-located towards the right hand side of the model. (a) Initial receiver geometry, (b) initial receiver density, (c) optimized receiver density, (d) optimized receiver geometry.

240x54mm (300 x 300 DPI)

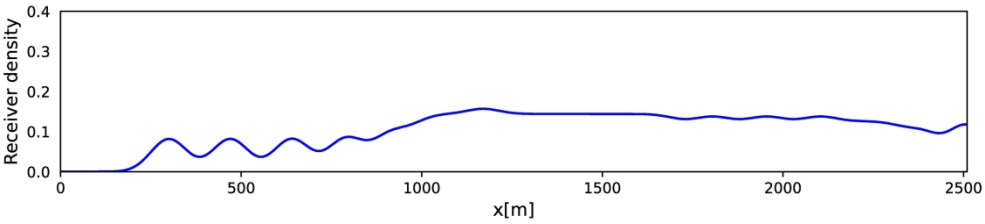

Figure 10c. Optimized receiver geometry for the model in Figure \ref{fig:Figure9_v}. The receivers are located at the surface $z=0$ m. After optimization, the receivers are re-located towards the right hand side of the model. (a) Initial receiver geometry, (b) initial receiver density, (c) optimized receiver density, (d) optimized receiver geometry.

238x56mm (300 x 300 DPI)

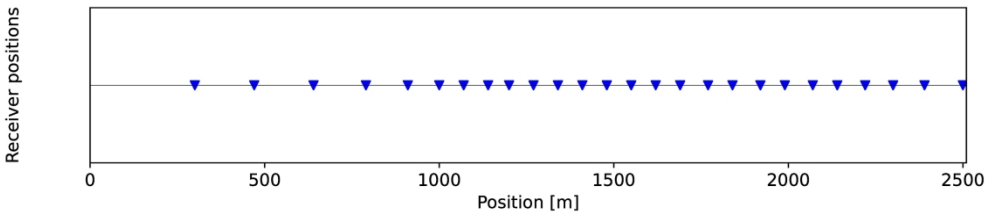

Figure 10d. Optimized receiver geometry for the model in Figure \ref{fig:Figure9_v}. The receivers are located at the surface $z=0$ m. After optimization, the receivers are re-located towards the right hand side of the model. (a) Initial receiver geometry, (b) initial receiver density, (c) optimized receiver density, (d) optimized receiver geometry.

246x57mm (300 x 300 DPI)

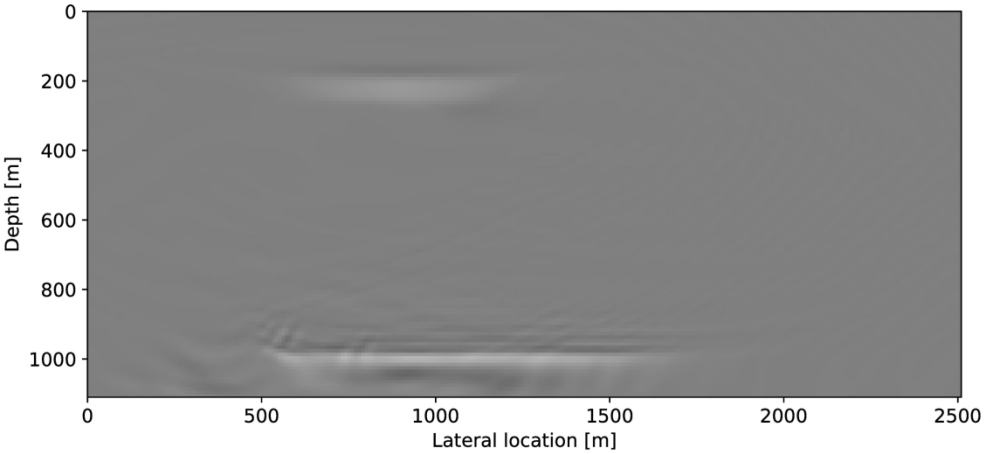

Figure 11a. Imaging the model in Figure \ref{fig:Figure9_v}. (a) Using the initial geometry in Figure~\ref{fig:Figure10A_v}. (b) Using the optimized geometry in Figure~\ref{fig:Figure10D_v}. (c) Comparison of target functions.

225x105mm (300 x 300 DPI)

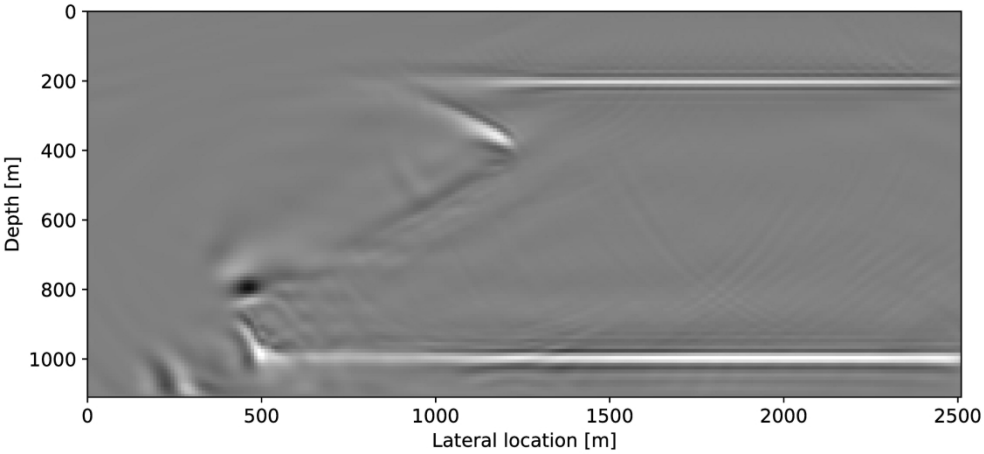

Figure 11b. Imaging the model in Figure \ref{fig:Figure9_v}. (a) Using the initial geometry in Figure~\ref{fig:Figure10A_v}. (b) Using the optimized geometry in Figure~\ref{fig:Figure10D_v}. (c) Comparison of target functions.

225x105mm (300 x 300 DPI)

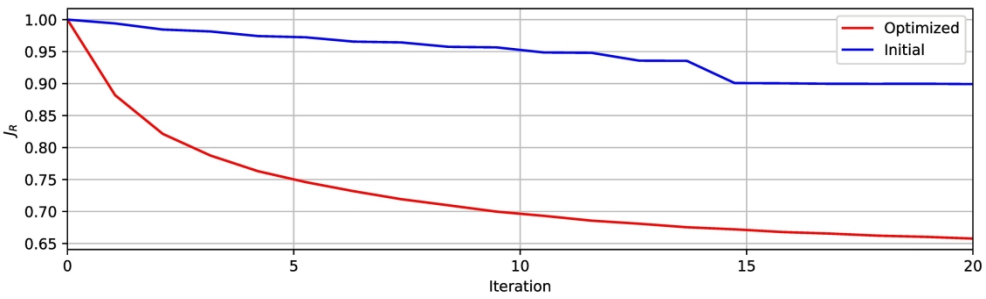

Figure 11c. Imaging the model in Figure \ref{fig:Figure9_v}. (a) Using the initial geometry in Figure~\ref{fig:Figure10A_v}. (b) Using the optimized geometry in Figure~\ref{fig:Figure10D_v}. (c) Comparison of target functions.

239x73mm (300 x 300 DPI)

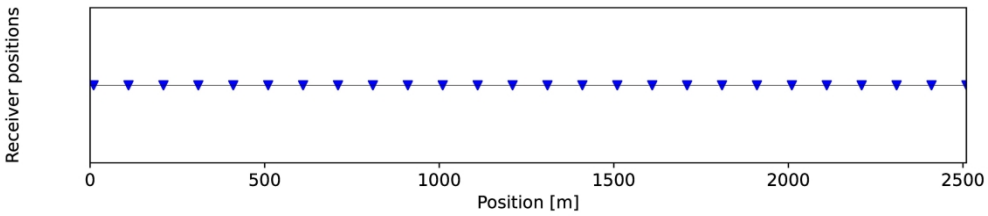

Figure 12a. Optimized receiver geometry for the model in Figure \ref{fig:Figure9_v}. The receivers are located at the surface $z=0$ m. After optimization, the receivers are re-located towards the right hand side of the model. (a) Initial receiver geometry, (b) initial receiver density, (c) optimized receiver density, (d) optimized receiver geometry.

246x57mm (300 x 300 DPI)

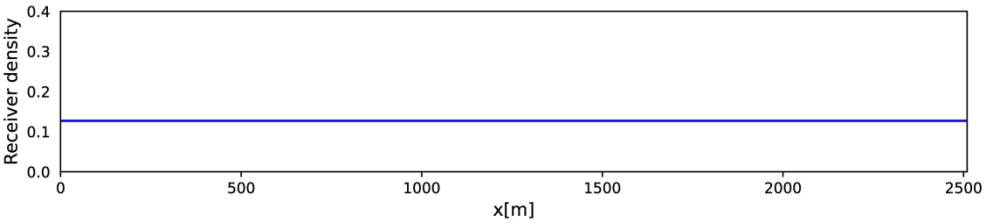

Figure 12b. Optimized receiver geometry for the model in Figure \ref{fig:Figure9_v}. The receivers are located at the surface $z=0$ m. After optimization, the receivers are re-located towards the right hand side of the model. (a) Initial receiver geometry, (b) initial receiver density, (c) optimized receiver density, (d) optimized receiver geometry.

238x56mm (300 x 300 DPI)

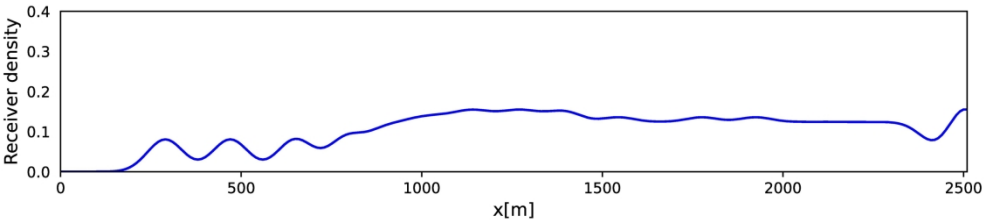

Figure 12c. Optimized receiver geometry for the model in Figure \ref{fig:Figure9_v}. The receivers are located at the surface $z=0$ m. After optimization, the receivers are re-located towards the right hand side of the model. (a) Initial receiver geometry, (b) initial receiver density, (c) optimized receiver density, (d) optimized receiver geometry.

238x56mm (300 x 300 DPI)

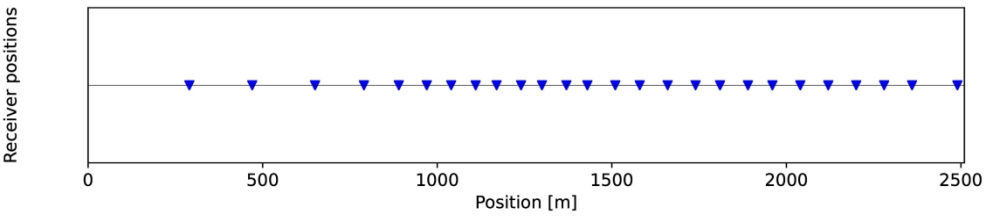

Figure 12d. Optimized receiver geometry for the model in Figure \ref{fig:Figure9_v}. The receivers are located at the surface $z=0$ m. After optimization, the receivers are re-located towards the right hand side of the model. (a) Initial receiver geometry, (b) initial receiver density, (c) optimized receiver density, (d) optimized receiver geometry.

246x57mm (300 x 300 DPI)

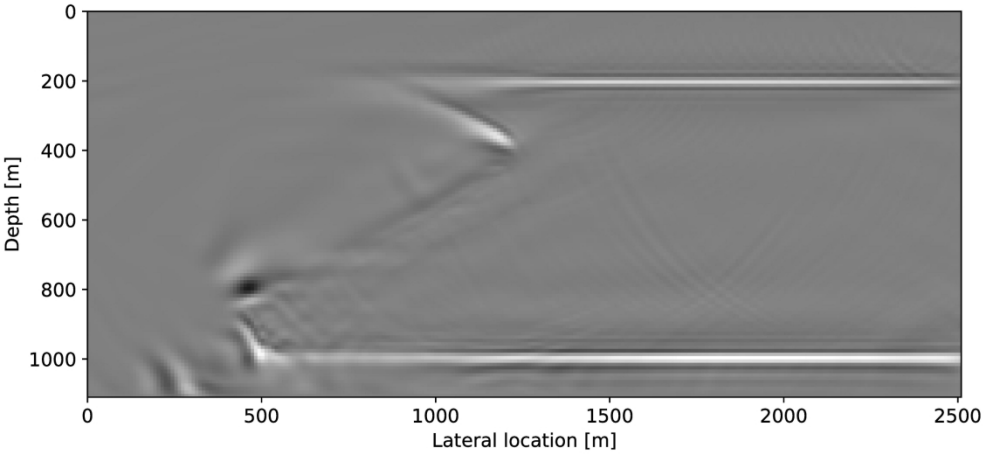

Figure 13a. Imaging the model in Figure \ref{fig:Figure9_v}. (a) Using the initial geometry in Figure~\ref{fig:Figure12A_v}. (b) Using the optimized geometry in Figure~\ref{fig:Figure12D_v}. (c) Amplitude difference between (a) and (b). (d) Comparison of target functions. The target function is always lower for the optimized geometry than for the uniform geometry.

225x105mm (300 x 300 DPI)

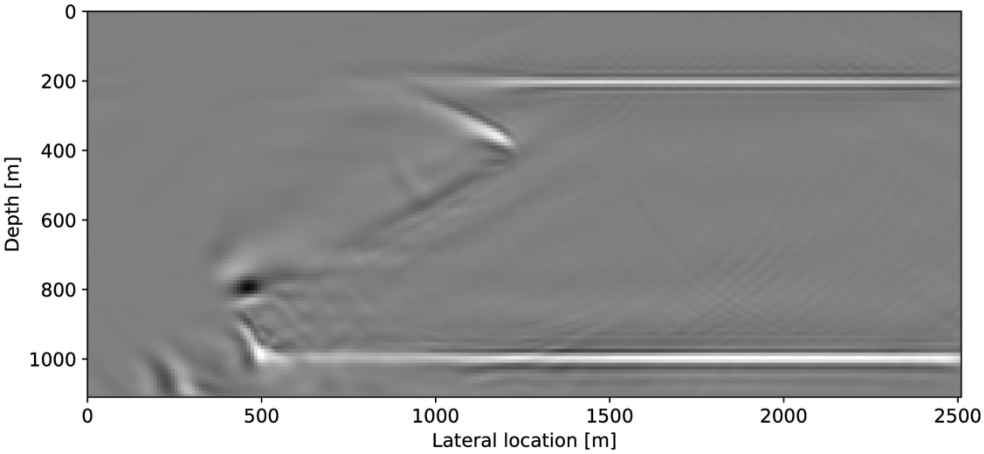

Figure 13b. Imaging the model in Figure \ref{fig:Figure9_v}. (a) Using the initial geometry in Figure~\ref{fig:Figure12A_v}. (b) Using the optimized geometry in Figure~\ref{fig:Figure12D_v}. (c) Amplitude difference between (a) and (b). (d) Comparison of target functions. The target function is always lower for the optimized geometry than for the uniform geometry.

225x105mm (300 x 300 DPI)

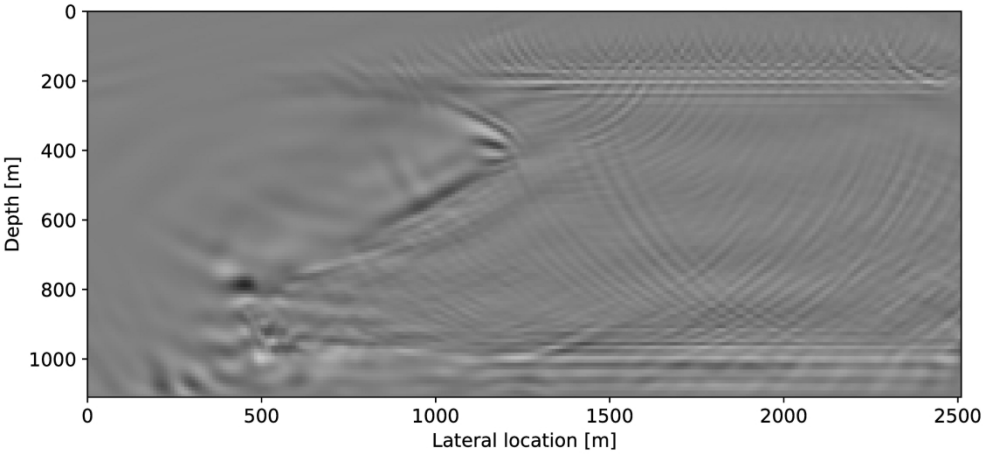

Figure 13c. Imaging the model in Figure \ref{fig:Figure9_v}. (a) Using the initial geometry in Figure~\ref{fig:Figure12A_v}. (b) Using the optimized geometry in Figure~\ref{fig:Figure12D_v}. (c) Amplitude difference between (a) and (b). (d) Comparison of target functions. The target function is always lower for the optimized geometry than for the uniform geometry.

225x105mm (300 x 300 DPI)

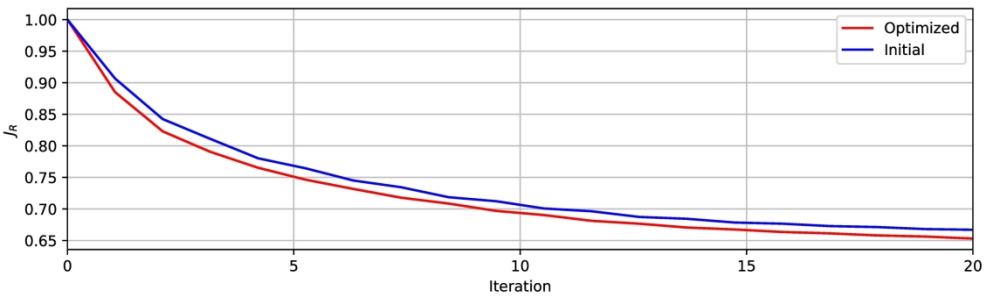

Figure 13d. Imaging the model in Figure \ref{fig:Figure9_v}. (a) Using the initial geometry in Figure~\ref{fig:Figure12A_v}. (b) Using the optimized geometry in Figure~\ref{fig:Figure12D_v}. (c) Amplitude difference between (a) and (b). (d) Comparison of target functions. The target function is always lower for the optimized geometry than for the uniform geometry.

239x73mm (300 x 300 DPI)

DATA AND MATERIALS AVAILABILITY

Data associated with this research are confidential and cannot be released.

DOI:10.1190/geo2022-0313.1